Nature Communications

https://doi.org/10.1038/s41467-026-71270-w

Article in Press

Spatiotemporal dynamics of the human cortical functional hierarchy across the lifespan

Received: 4 May 2025

Accepted: 16 March 2026

Cite this article as: Li, Q., Liang, X., Zeng, D. *et al.* Spatiotemporal dynamics of the human cortical functional hierarchy across the lifespan. *Nat Commun* (2026). https://doi.org/10.1038/s41467-026-71270-w

Qiongling Li, Xinyuan Liang, Debin Zeng, Tengda Zhao, Xuhong Liao, Gaolang Gong, Qian Wang, Chenxuan Pang, Qian Yu, Xiaoxi Dong, Yirong He, Yanchao Bi, Pindong Chen, Rui Chen, Yuan Chen, Taolin Chen, Jingliang Cheng, Yuqi Cheng, Zaixu Cui, Zhengjia Dai, Yao Deng, Yuyin Ding, Qi Dong, Dingna Duan, Jia-Hong Gao, Qiyong Gong, Ying Han, Zaizhu Han, Chu-Chung Huang, Ruiwang Huang, Ran Huo, Lingjiang Li, Ching-Po Lin, Qixiang Lin, Bangshan Liu, Chao Liu, Ningyu Liu, Ying Liu, Yong Liu, Jing Lu, Leilei Ma, Weiwei Men, Shaozheng Qin, Wen Qin, Jiang Qiu, Shijun Qiu, Tianmei Si, Shuping Tan, Yanqing Tang, Sha Tao, Dawei Wang, Fei Wang, Jiali Wang, Pan Wang, Xiaoqin Wang, Yanpei Wang, Dongtao Wei, Yankun Wu, Peng Xie, Xiufeng Xu, Yuehua Xu, Zhilei Xu, Liyuan Yang, Chunshui Yu, Huishu Yuan, Zilong Zeng, Haibo Zhang, Xi Zhang, Gai Zhao, Yanting Zheng, Suyu Zhong, MCADI, DIDA-MDD Working Group, Mingrui Xia, Shuyu Li & Yong He

Title

Spatiotemporal dynamics of the human cortical functional hierarchy across the lifespan

Author list

Qiongling Li[1,2,3], Xinyuan Liang[1,2,3], Debin Zeng[4], Tengda Zhao[1,2,3], Xuhong Liao[5], Gaolang Gong[1,2,3,6], Qian Wang[1,2,3], Chenxuan Pang[1,2,3], Qian Yu[1,2,3], Xiaoxi Dong[1], Yirong He[1], Yanchao Bi[1,7,8], Pindong Chen[9], Rui Chen[1], Yuan Chen[10,11,12,13], Taolin Chen[14,15,16], Jingliang Cheng[10,11,12,13], Yuqi Cheng[17], Zaixu Cui[6], Zhengjia Dai[1,2,3], Yao Deng[1], Yuyin Ding[1], Qi Dong[1], Dingna Duan[1,2,3], Jia-Hong Gao[8,18,19], Qiyong Gong[14,15,16], Ying Han[20], Zaizhu Han[1,3], Chu-Chung Huang[21], Ruiwang Huang[1,3,22], Ran Huo[23], Lingjiang Li[24,25], Ching-Po Lin[26,27], Qixiang Lin[1,2,3], Bangshan Liu[24,25], Chao Liu[1,3], Ningyu Liu[1], Ying Liu[23], Yong Liu[28], Jing Lu[1], Leilei Ma[1], Weiwei Men[18,19], Shaozheng Qin[1,2,3,6], Wen Qin[29], Jiang Qiu[30,31,32], Shijun Qiu[33,34], Tianmei Si[35], Shuping Tan[36], Yanqing Tang[37], Sha Tao[1], Dawei Wang[38], Fei Wang[39], Jiali Wang[1], Pan Wang[40], Xiaoqin Wang[30,31], Yanpei Wang[1], Dongtao Wei[30,31], Yankun Wu[35], Peng Xie[41,42], Xiufeng Xu[43], Yuehua Xu[1,2,3], Zhilei Xu[1,2,3], Liyuan Yang[1,2,3], Chunshui Yu[29], Huishu Yuan[23], Zilong Zeng[1,2,3], Haibo Zhang[1], Xi Zhang[44], Gai Zhao[1], Yanting Zheng[33], Suyu Zhong[28], MCADI[45], DIDA-MDD Working Group[45], Mingrui Xia[1,2,3,*], Shuyu Li[1,*], and Yong He[1,2,3,6,*]

[1] State Key Laboratory of Cognitive Neuroscience and Learning, Beijing Normal University, Beijing, China;
[2] Beijing Key Laboratory of Brain Imaging and Connectomics, Beijing Normal University, Beijing, China;
[3] IDG/McGovern Institute for Brain Research, Beijing Normal University, Beijing, China;
[4] Beijing Advanced Innovation Center for Biomedical Engineering, School of Biological Science & Medical Engineering, Beihang University, Beijing, China;
[5] School of Systems Science, Beijing Normal University, Beijing, China;
[6] Chinese Institute for Brain Research, Beijing, China;
[7] School of Psychological and Cognitive Sciences and Beijing Key Laboratory of Behavior and Mental Health, Peking University, Beijing, China;
[8] IDG/McGovern Institute for Brain Research, Peking University, Beijing, China;
[9] Brainnetome Center & National Laboratory of Pattern Recognition, Institute of Automation, Chinese Academy of Sciences, Beijing, China;
[10] Department of Magnetic Resonance Imaging, The First Affiliated Hospital of Zhengzhou University, Zhengzhou, China;
[11] Henan Engineering Technology Research Center for detection and application of brain function, Zhengzhou, China;
[12] Key Laboratory for functional magnetic resonance imaging and molecular imaging of Henan Province, Zhengzhou, China;
[13] Henan Engineering Research Center of medical imaging intelligent diagnosis and treatment, Zhengzhou, China
[14] Department of Radiology, Huaxi MR Research Center (HMRRC), Institute of Radiology and Medical Imaging, West China Hospital of Sichuan University, Chengdu, Sichuan, China;
[15] Psychoradiology Key Laboratory of Sichuan Province, West China Hospital of Sichuan University, Chengdu, Sichuan, China;
[16] Xiamen Key Lab of Psychoradiology and Neuromodulation, Department of Radiology, West China Xiamen Hospital of Sichuan University, Xiamen, Fujian, China;
[17] Affiliated Mental Health Center & Hangzhou Seventh People's Hospital, Zhejiang University School of Medicine, Hangzhou, Zhejiang, China;
[18] Center for MRI Research, Academy for Advanced Interdisciplinary Studies, Peking University, Beijing, China;
[19] Beijing City Key Laboratory for Medical Physics and Engineering, Institute of Heavy Ion Physics, School of

Physics, Peking University, Beijing, China;
[20] Department of Neurology, Xuanwu Hospital of Capital Medical University, Beijing, China;
[21] Key Laboratory of Brain Functional Genomics (Ministry of Education), Affiliated Mental Health Center (ECNU), School of Psychology and Cognitive Science, East China Normal University, Shanghai, China;
[22] School of Psychology, South China Normal University, Guangzhou, China;
[23] Department of Radiology, Peking University Third Hospital, Beijing, China;
[24] Department of Psychiatry, and National Clinical Research Center for Mental Disorders, The Second Xiangya Hospital of Central South University, Changsha, China;
[25] Mental Health Institute of Central South University, China National Technology Institute on Mental Disorders, Hunan Technology Institute of Psychiatry, Hunan Key Laboratory of Psychiatry and Mental Health, Hunan Medical Center for Mental Health, Changsha, China;
[26] Institute of Neuroscience, National Yang Ming Chiao Tung University, Taipei, China;
[27] Department of Education and Research, Taipei City Hospital, Taipei, China;
[28] Center for Artificial Intelligence in Medical Imaging, School of Artificial Intelligence, Beijing University of Posts and Telecommunications, Beijing, China;
[29] Department of Radiology & Tianjin Key Lab of Functional Imaging & Tianjin Institute of Radiology & State Key Laboratory of Experimental Hematology, Tianjin Medical University General Hospital, Tianjin, China;
[30] Key Laboratory of Cognition and Personality (SWU), Ministry of Education, Chongqing, China;
[31] Department of Psychology, Southwest University, Chongqing, China;
[32] Southwest University Branch, Collaborative Innovation Center of Assessment Toward Basic Education Quality at Beijing Normal University, Chongqing, China;
[33] Department of Radiology, The First Affiliated Hospital of Guangzhou University of Chinese Medicine, Guangzhou, China;
[34] State Key Laboratory of Traditional Chinese Medicine Syndrome, Guangzhou, China
[35] Peking University Sixth Hospital, Peking University Institute of Mental Health, NHC Key Laboratory of Mental Health (Peking University), National Clinical Research Center for Mental Disorders (Peking University Sixth Hospital), Peking University, Beijing, China;
[36] Beijing Huilongguan Hospital, Peking University Huilongguan Clinical Medical School, Beijing, China;
[37] Department of Psychiatry, Shengjing Hospital of China Medical University, Shenyang, China;
[38] Department of Radiology, Qilu Hospital of Shandong University, Ji'nan, China;
[39] Department of Psychiatry, The First Affiliated Hospital of China Medical University, Shenyang, China;
[40] Department of Neurology, Tianjin Huanhu Hospital, Tianjin University, Tianjin, China;
[41] Chongqing Key Laboratory of Neurobiology, Chongqing, China;
[42] Department of Neurology, The First Affiliated Hospital of Chongqing Medical University, Chongqing, China;
[43] Department of Psychiatry, First Affiliated Hospital of Kunming Medical University, Kunming, Yunnan, China;
[44] Department of Neurology, the Second Medical Centre, National Clinical Research Centre for Geriatric Diseases, Chinese PLA General Hospital, Beijing, China;
[45] A list of authors and affiliations is provided in the supplementary material.

[*] Correspondence to: Yong He, yong.he@bnu.edu.cn; Shuyu Li, shuyuli@bnu.edu.cn; Mingrui Xia, mxia@bnu.edu.cn.

Keywords: cortical hierarchy, default-mode, gradient, sensorimotor-association axis, functional connectome

Abstract

The human cortical functional hierarchy, spanning from primary sensorimotor to transmodal association regions, represents a fundamental principle of brain organization. Here, we show lifespan changes in the sensorimotor-association (S-A) gradient in the cortical functional hierarchy using multimodal neuroimaging data from 33,247 participants aged 32 postmenstrual weeks to 80 years. We identify three critical neurodevelopmental milestones: initiation (third trimester to perinatal period), establishment (infancy to early childhood), and expansion-stabilization (late childhood to adulthood). Pronounced gradient changes are predominantly observed during the first decade, with continued refinement extending into mid-adulthood. Spatiotemporally heterogeneous growth patterns in functional gradients align with evolutionary hierarchies, segregation–integration dynamics, structural maturation, and cognitive spectrum development, proceeding along a dominant S-A growth axis. These findings establish a unified neurodevelopmental framework that links connectome gradient dynamics to multifaceted functional and structural properties, advancing our understanding of cortical hierarchy maturation across the lifespan.

Introduction

The functional hierarchy in the human cerebral cortex serves as a fundamental principle of brain organization. At the macroscale, functional connectome gradients provide a critical framework for delineating the intrinsic spatial topography of the brain [1,2]. Among these gradients, the sensorimotor-association (S-A) gradient represents the principal axis of the cortical functional hierarchy, spanning from primary and unimodal regions to transmodal association regions [3]. This gradient axis is anchored at its extremes by the most distal cortical regions, with multimodal regions occupying intermediate positions along the continuum [1,3,4]. This cortex-wide organization ensures the spatial continuity of information transfer across adjacent areas, facilitating a continuous cognitive spectrum ranging from basic sensory processing, perception, and motor action to abstract cognition along the cortical mantle [3,5]. Notably, the S-A gradient axis aligns with spatial variations in key neurobiological properties [2], including cortical thickness [6,7], intracortical myelination [8–10], and gene expression signatures [11,12]. Perturbations in this hierarchical organization along the S-A axis have been linked to the pathophysiology of neuropsychiatric disorders [13–17]. However, despite its central role in cortical organization, the spatiotemporal dynamics of S-A axis across the lifespan, as well as its coevolution with multifaceted structural properties, remain poorly understood. Addressing these knowledge gaps is essential for advancing our understanding of the principles governing cortical functional organization and their implications for both normative cognition and the pathogenesis of neuropsychiatric disorders.

The development patterns of the S-A axis have garnered considerable interests [16,18–23]. Emerging evidence suggests that the anterior–posterior gradient configuration begins to form during prenatal development [18,19], manifesting as an immature S-A hierarchy. Although the S-A axis becomes discernible during preschool years [16], its global and regional topography undergoes gradual refinement throughout childhood and adolescence [20,21], continuing into adulthood [22,23]. This protracted process facilitates progressive segregation and integration, supporting the emergence of advanced cognitive abilities [19,20]. Despite these advances, critical gaps remain in the lifespan maturation of the functional hierarchy. First, most existing studies of the functional hierarchy have focused on discrete developmental stages (e.g., the third trimester [19], neonatal period [18], adolescence [20,21] and adulthood [3,22]), resulting in a fragmented perspective that obscures nonlinear gradient dynamics across the full age continuum. Moreover, prior work has often been limited by small (e.g., $N < 100$) [18,19] or modest (N = hundreds to thousands) [16,20–22] sample sizes, along with a predominant reliance on linear modelling for gradient development [19,20,22]. Although a recent study [23] established a continuous, nonlinear mapping of functional gradients from birth to 100 years of age, the developmental patterns remain constrained by a modest sample size ($N = 3,556$) and particularly sparse data coverage during childhood. Second, previous studies have failed to delineate how functional hierarchies coevolve with specific structural and geometric features, such as cortical thickness [2,6,7], intracortical myelination [2,8,9], and intrinsic geometry [3,24], across the lifespan. While the S-A axis aligns spatially with these structural attributes in adult brains, the developmental functional-structural synchrony remains unclear. A previous study [23] linked lifespan changes in functional gradients with a composite structural gradient, but its analysis strategy that integrates multiple structural features into a morphometric similarity network, did not directly assess how specific structural properties shape functional gradients. Therefore, addressing these fundamental questions will require large-scale, lifespan-spanning multimodal neuroimaging datasets, harmonized processing pipelines and non-

linear analytical frameworks capable of modelling lifespan trajectories of functional gradients, structural properties, and their dynamic interactions.

To address these challenges, we utilized multimodal neuroimaging data from 33,247 participants aged between 32 postmenstrual weeks (PMW) and 80 years, collected at 132 global sites. By employing a diffusion map embedding approach [3,25], we identified the S-A gradient of the functional connectome. Specifically, we sought to i) delineate neurodevelopmental milestones of the spatial organization and extent of the S-A gradient axis, ii) map nonlinear trajectories of the S-A axis at the global, system, and regional levels via generalized additive models for location, scale, and shape (GAMLSS) [26], iii) investigate how lifespan changes in the functional gradient axis correlate with multifaceted structural and geometric hierarchies, and iv) conduct a NeuroSynth-based meta-analysis [27] to examine the alignment of developing S-A gradient with adult cognitive spectrum. These integrative multimodal and multifaceted analyses provide insights into the principles governing the lifespan maturation of the cortical hierarchy.

Results

Following a rigorous quality control protocol [28], we analyzed structural MRI and task-free functional MRI data from 33,247 participants aged 32 PMW and 80 years. Detailed demographic information, acquisition parameters, quality control procedures, and preprocessing protocols are described in the Methods section and in our prior work [28]. Preprocessed functional data were mapped onto cortical surfaces, and functional connectomes were constructed by computing pairwise correlation coefficients between the time series of all cortical surface vertices (4,609 × 4,609) [28]. Using well-established diffusion map embedding techniques [3,25], we decomposed both age-specific, group-level connectomes and person-specific connectomes into multiple gradients representing functional connectivity variations across the brain. Our primary focus was on the lifespan growth of the principal S-A gradient, given its pivotal role in cognition [3], development [19–21,29], disease [13–17], and evolution [30,31].

Topographically distinct growth stages of the S-A gradient axis

We investigated whether the S-A gradient undergoes distinct stages across the lifespan using both group- and individual-level analyses. We first examined how the hierarchical S-A axis emerges during early development and matures into a canonical gradient of cortical functional organization. To this end, we divided the lifespan into 26 distinct age groups [28] and generated 26 age-specific, group-based functional connectomes. Age ranges were defined with finer intervals for early developmental stages, reflecting rapid changes, and broader intervals for adulthood, reflecting relative stability. Initially, the connectome gradient manifests as an anterior–posterior axis, which gradually evolves into the canonical S-A axis that spans from primary and unimodal regions at one end to transmodal frontal, temporal, and parietal association regions at the other end (Fig. 1a). This maturation process highlights substantial reorganization of the functional topography of the S-A axis over the lifespan. To delineate the temporal sequence of S-A axis establishment and maturation, we performed K-means clustering analysis on the 26 group-based gradient maps (Fig. 1b & Supplementary Fig. 1). This analysis revealed that functional gradients across age groups are optimally clustered into three distinct stages (Fig. 1b, c).

i) Phase I: Initiation. This phase covers the third trimester and perinatal period (approximately 32 PMW to 1 month). During this stage, cortical topography begins to differentiate functionally

between anterior and posterior regions, accompanied by a gradual broadening of the gradient range (Fig. 1a, d).

ii) Phase II: Establishment. Spanning infancy to early childhood (approximately 3 months to 4 years), this phase is characterized by a remarkable transition in functional topography, as the anterior–posterior gradient is replaced by the S-A gradient (Fig. 1a, d). Early in infancy (approximately 3–9 months), the anterior–posterior gradient range narrows, and multiple peaks emerge along this axis (Fig. 1a, d), reflecting increased functional differentiation in cortical organization. By late infancy and early childhood (approximately 12 months to 4 years), the canonical S-A axis is established, as evidenced by two distinct peaks in the ridge distribution corresponding to the sensorimotor and association cortices, respectively (Fig. 1a, d).

iii) Phase III: Expansion and stability. This phase extends from late childhood through adolescence and adulthood (5 years to 80 years). During late childhood and adolescence, the cortical topography of the S-A gradient becomes clearly discernible and undergoes progressive expansion in the gradient range, followed by a prolonged period of relative stability in cortical topography over several decades (Fig. 1a, c, and d). Notably, it is during adolescence that the S-A gradient solidifies as the dominant principal gradient (Supplementary Fig. 2).

We also mapped the visual-sensorimotor (V-S) and the modulation-representation (M-R) gradients maps across the lifespan. The V-S gradient emerges from an early anterior-posterior pattern before birth and refines progressively from infancy through adulthood. In contrast, the M-R gradient is preliminarily established by early childhood and gradually stabilizes into its mature configuration during adolescence and adulthood (Supplementary Fig. 3-4). We further computed the spatial similarity between these group-specific gradients and the canonical S-A axis[2] and observed that it increased steadily with age in Phase I, slightly decreased in Phase II, and eventually stabilized at a high level in Phase III (Supplementary Fig. 5). Notably, the slight decrease observed during Phase II is accompanied by a period of transient instability in cortical gradient organization, during which the dorsal attention (DA) and ventral attention (VA) systems show temporary changes in their alignment with large-scale gradients, consistent with broader shifts in gradient organization (Supplementary Fig. 6). This trend supports the view that the S-A axis is not fully established at birth but rather emerges through progressive reorganization. The three developmental phases were also identified through individual-level gradient clustering without predefined age bins, within-age-group-harmonized analysis, and within-dataset replication analyses (Supplementary Fig. 7-11). Nonetheless, the definitions and age boundaries of developmental phases could be influenced by methodological choices such as site effects and clustering analysis.

Normative growth of the S-A gradient axis across lifespan

We systematically delineated the lifespan growth trajectories of the S-A gradient at the global, system and regional levels. Lifespan growth curves were modelled using GAMLSS [26], with age included as a smoothing term, sex and in-scanner head motion as fixed effects, and site as a random effect. The growth rates were derived as the first derivatives of these growth curves.

i) Global level. Three global gradient measures [14] were evaluated for the S-A axis: the explanation ratio, which measures the percentage of variance in the connectivity profile accounted for by the gradient; the gradient range, which measures the difference between the two

extremes of the gradient; and the standard deviation, which measures the heterogeneity of gradient values across the cortex. The explanation ratio of the S-A gradient exhibited a prolonged period of nonlinear increase, peaking in the late fifth decade (46.8 years, 95% bootstrap confidence interval (CI): 43.4-49.9), followed by a gradual decline (Fig. 2a). Similarly, both the gradient range and standard deviation of the S-A axis demonstrated nonlinear increases, peaking in the fourth decade (gradient range: 32.0 years, 95% bootstrap CI: 29.2-36.1; standard deviation: 36.2 years, 95% bootstrap CI: 33.9-38.8; Fig. 2a).

ii) System level. We examined the lifespan growth trajectories of the gradient range, standard deviation, and gradient values for each system within the S-A axis. Here, individual-level functional systems were derived by integrating age-specific Yeo 7-network atlases with a person-specific iterative algorithm [28,32,33]. Generally, the growth curves for the gradient range and standard deviation across all brain systems (Fig. 2b) mirrored the patterns observed at the global level (Fig. 2a). Notably, the default-mode network (DMN) and frontoparietal network (FPN) exhibited higher gradient ranges and standard deviations, whereas the sensorimotor systems presented lower values throughout the lifespan, reflecting greater functional differentiation in association cortices than in primary cortices. Gradient value analysis revealed distinct nonlinear growth patterns across systems (Supplementary Fig. 12). Specifically, the visual, ventral attention, and dorsal attention systems reach their extreme values during adolescence, whereas the DMN, FPN, and somatomotor systems exhibited more protracted trajectories, reaching their extreme values in the fourth decade of life (Fig. 2c). To further characterize the distribution of gradient values across systems along the S-A axis, we performed a descriptive exclusion analysis by iteratively removing each system's vertices and quantifying the shift in mean gradient value normalized by vertex count. This analysis revealed system-specific differences in gradient distribution across developmental stages (repeated-measures analysis of variance (ANOVA), $F_{interaction}$ (12,199460) = 341.8, $p < 0.001$; Fig. 2d and Supplementary Tables 1-4). During Phase I and Phase II, excluding somatomotor-associated vertices produced the largest shifts in the mean gradient value (all post-hoc $ps < 0.001$), whereas during Phase III, the largest shifts resulted from excluding DMN-associated vertices (all post-hoc $ps < 0.001$).

iii) Regional level. We characterized the regional maturation processes of gradient values along the S-A axis. The most pronounced changes occurring in the first decade of life and continued into at least early adulthood (Fig. 2e). Notably, substantial changes in regional gradient values were observed not only at the two extremes of the S-A axis (e.g., posterior DMN and lateral visual regions), but also at intermediate positions (e.g., ventral attention regions such as the insula and dorsal anterior cingulate, and dorsal attention regions such as the superior frontal and parietal cortices). To elucidate the spatiotemporal growth principles across the cortex, we applied principal component analysis (PCA) to the fitted growth curves of all vertices. The first principal component accounted for 65.4% of the variance in the regional gradient profiles (Fig. 2f), representing the dominant lifespan growth axis. Along this axis, distinct growth patterns of gradient values were evident in the sensorimotor and association cortices (Fig. 2f). This dominant lifespan growth axis closely aligned with the S-A gradient axis (Spearman's $\rho = 0.91$, $p_{spin} < 0.001$; Supplementary Fig. 13) and the macaque-to-human evolutionary hierarchy [30] (Spearman's $\rho = 0.32$, $p_{spin} = 0.02$; Fig. 2g).

Lifespan association between the S-A axis and segregation/integration

The hierarchical organization of cortical architecture facilitates efficient information transfer

between sensorimotor and association regions [4], which is critically dependent on the dynamic equilibrium between functional segregation and integration [34]. Here, we investigated the lifespan coupling between S-A gradient and segregation-integration dynamics via graph theoretical analysis. Our findings revealed that the global clustering coefficient (C_p, segregation index) and inverse characteristic shortest path length ($1/L_p$, integration index) exhibited distinct nonlinear maturation trajectories: the C_p demonstrated an initial increase, peaking in early adulthood (32.7 years, 95% bootstrap CI: 30.7–35.0), followed by a gradual decline (Fig. 3a), whereas $1/L_p$ showed an initial decease, reaching its minimum in mid-adulthood (41.1 years, 95% bootstrap CI: 39.6–42.7), before subsequently increasing (Fig. 3b).

Regional clustering coefficient ($C_{p\text{-node}}$) decreased from primary to transmodal association regions, independent of age (Fig. 3c). While sensorimotor regions presented the highest levels of local clustering throughout the cortex, these primary regions still presented a nonlinear increase in functional specialization from infancy through early adulthood, followed by a decline in later aging stages (Fig. 3c). Regional efficiency ($1/L_{p\text{-node}}$) demonstrated substantial developmental changes primarily during the first decade of life: sensorimotor regions exhibited peak efficiency during infancy, which gradually decreased with development, whereas association regions showed marked increases in efficiency, becoming dominant from childhood through adolescence and adulthood (Fig. 3d). This pattern reflects a developmental trajectory of reduced integration in primary regions alongside enhanced integration in association regions as functional specialization progresses. Spatial correlation analyses revealed significant associations between clustering coefficient maps and functional gradient maps across the lifespan (all $p_{spin} < 0.05$, FDR-corrected; Supplementary Fig. 14a), whereas regional efficiency showed no significant correlations (all $p_{spin} > 0.05$, FDR-corrected; Supplementary Fig. 14b). This finding suggests that functional gradient maturation is more strongly coupled with functional segregation than with integration.

Finally, we applied PCA to the fitted growth curves of regional clustering ($C_{p\text{-node}}$) and efficiency ($1/L_{p\text{-node}}$) values across all vertices. The first PCA components accounted for 74.9% and 57.6% of the variance in the regional clustering and efficiency growth profiles, respectively (Fig. 3e, f). Notably, both regional clustering and efficiency demonstrated spatially heterogeneous maturation patterns across the lifespan. The lifespan S-A growth axes of regional clustering and efficiency were correlated with those of the canonical connectome gradient (regional clustering: Spearman's $\rho = -0.78$, $p_{spin} < 0.001$; Fig. 3g; regional efficiency: Spearman's $\rho = 0.19$, $p_{spin} = 0.02$; Fig. 3h).

To complement the graph-theoretical results, we additionally examined averaged within- and between-system FC across vertices [35,36]. Both measures showed systematic variation along the S-A axis and were significantly coupled with S-A gradient maturation across the lifespan (Supplementary Fig. 15-16). PCA further revealed that developmental axes of both measures were correlated with the growth axis of the S-A gradient (within-system FC: Spearman's $\rho = -0.51$, $p_{spin} < 0.001$; between-system FC: Spearman's $\rho = -0.56$, $p_{spin} < 0.001$; Supplementary Fig. 15). These findings highlight that the lifespan maturation of the S-A gradient and functional segregation/integration proceed in a convergent manner along an overarching, hierarchical growth axis.

Lifespan association between the S-A axis and structural hierarchies

We investigated how the S-A gradient axis coevolves with multifaceted geometric and structural features across the lifespan. Our investigation focused on three features: geometric distance [3,24], macrostructural cortical thickness [7], and intracortical T1w/T2w contrast ratio [9].

For geometric distance analysis, we first identified vertices within the top and bottom 5% of S-A gradient values (Fig. 4a), representing regions of maximal functional differentiation. For each individual, we calculated the mean normalized geometric distances between paired vertices with extreme gradient values. This geometric distance exhibited a nonlinear trajectory across the lifespan, peaking during young adulthood (20.7 years, 95% bootstrap CI: 17.2–23.2), followed by a gradual decline (Fig. 4b). Cosine similarity analysis between geometric distances and gradient value differences revealed robust geometry–hierarchy coupling ($r > 0.88$ across all ages), with similarity decreasing until late adolescence (peak at 17.0 years, 95% bootstrap CI: 14.3-19.5) and stabilizing thereafter (Fig. 4c). These findings suggest that while geometric constraints strongly influence the functional hierarchy, their influence gradually diminishes during development.

For structural analyses, our investigation revealed the following key findings: First, transmodal association cortices exhibited greater cortical thickness and reduced T1w/T2w contrast ratio than did sensorimotor cortices throughout the lifespan (Fig. 4d, e), which is consistent with established S-A axis characteristics in adults[7,10]. Structural changes were most pronounced during the first decade of life and continued into the third decade, with distinct regional patterns: cortical thinning predominated in transmodal association cortices, whereas the primary visual cortex showed thickening (Fig. 4d), and T1w/T2w contrast ratio patterns revealed decreased levels in paralimbic association cortices (e.g., insula and dorsal anterior cingulate) alongside increased levels in sensorimotor regions (Fig. 4e). Second, spatial correlation analyses revealed significant associations between functional gradient maps and both cortical thickness and intracortical T1w/T2w contrast ratio maps across the lifespan (all $p_{spin} < 0.05$, FDR-corrected; Supplementary Fig. 17), with the strongest correlations occurring during the first two decades. Third, PCA of the structural growth curves revealed that the first principal components explained 97.3% and 89.0% of the variance in the cortical thickness and intracortical T1w/T2w contrast ratio growth profiles, respectively (Fig. 4f, g). The cortical thickness growth axis exhibited a regionally heterogeneous pattern spanning from sensorimotor to association cortices (Fig. 4f), with a positive correlation with the functionally defined S-A growth axis (Spearman's $\rho = 0.36$, $p_{spin} < 0.001$; Fig. 4h). In contrast, the T1w/T2w contrast ratio-based growth axis extended from the sensorimotor cortices to paralimbic association cortices (e.g., the insula and cingulate cortex) (Fig. 4g) and was not correlated with either the lifespan growth axis of the functional gradient (Spearman's $\rho = 0.04$, $p_{spin} = 0.42$; Fig. 4i) or the cortical thickness (Spearman's $\rho = 0.01$, $p_{spin} = 0.25$). These findings collectively demonstrate that lifespan maturation of functional gradients is primarily coupled with cytoarchitectural development rather than myeloarchitectural development.

Lifespan S-A gradient alignment with adult cognitive spectrum

In adults, the S-A gradient axis supports a cognitive spectrum that spans from perception and action to abstract cognition [3]. However, how lifespan changes in the S–A axis align with this adult cognitive spectrum remains unknown. To address this issue, we conducted a cognitive

decoding meta-analysis on both group- and person-specific S-A gradients in the NeuroSynth database [27]. The dominant S-A gradient was first identified from young adult Human connectome project data (n=897) [37]. We then constructed a reference spectrum map comprising 24 cognitive terms distributed along the S-A axis (for details, see Methods). This reference map showed a clear continuum: perception and action terms anchored the primary/unimodal end, while abstract cognitive terms dominated the transmodal end (Fig. 5a), replicating earlier findings [3].

For group-level analysis, we generated cognitive spectrum maps along the S-A axis for each of the 26 age-specific groups via identical procedures to those used for reference map construction (Fig. 5a). We quantified two key metrics: i) the mean gradient bin width associated with cognitive terms, reflecting the degree of clustering of the corresponding brain areas along the S-A axis, and ii) the correlation between the median gradient bin of each term and its corresponding gradient percentile, reflecting the covariation between the cognitive and S-A axes (Fig. 5b, left panel). Our analyses revealed that compared with those of earlier developmental stages, Phase III (expansion and stability stage) presented narrower mean gradient widths (Kruskal–Wallis test, $\eta^2 = 0.62$, $p < 0.001$; post-hoc tests, both $p \leq 0.01$; Fig. 5b, middle panel) and stronger cognitive–gradient correlations (Kruskal–Wallis test, $\eta^2 = 0.73$, $p < 0.001$; post-hoc both $p \leq 0.002$; Fig. 5b, right panel). Individual-level analysis of the cognitive spectrum maps revealed that the mean term width decreased rapidly during early development and stabilized after adolescence (peak at 15.3 years, 95% bootstrap CI: 14.5–16.6; Fig. 5c), whereas the cognitive term–gradient correlations increased progressively, reaching maximal values in the third decade of life (29.3 years, 95% bootstrap CI: 26.1–31.8; Fig. 5c). Finally, quantitative comparison of group-based cognitive spectrum maps with the reference map via Dice coefficients revealed a progressive increase in similarity from the perinatal period through early adulthood, followed by a modest decline (Fig. 5d). Individual-level analysis revealed a similar developmental trajectory, with Dice coefficient peaking in the third decade (26.1 years, 95% bootstrap CI: 25.4–28.7; Fig. 5e). These results reveal a progressive strengthening of alignment between age-specific functional gradients and the adult cognitive spectrum, reflecting the developmental convergence of cortical organization toward adult cognitive-functional topography.

Sex differences in the lifespan S-A gradient

To investigate sex differences in the lifespan trajectory of the S-A gradient axis, we fitted GAMLSS models with a sex-by-age interaction term at the global, system, and regional levels. Globally, females showed higher explanation ratio and greater gradient range and variation across the lifespan than males (all $p < 0.05$, FDR-corrected, Supplementary Fig. 18a). At the system level, females also showed greater gradient ranges and variations than males (all $p < 0.001$, FDR-corrected, Supplementary Fig. 18b). Notably, in several systems, including visual, limbic, FPN, and DMN, females exhibited later peak ages than males (all $p < 0.001$, FDR-corrected, Supplementary Fig. 18c and Supplementary Table 5). Regionally, females showed higher gradient values in medial prefrontal and parietal regions and later temporal regions, whereas males exhibited higher values in the occipital regions ($p < 0.001$, FDR-corrected, Supplementary Fig. 18d). These findings indicate that sex differences in cortical hierarchy manifest not only in magnitude but also in developmental timing.

Sensitivity analyses

To validate the lifespan growth patterns of the S-A gradient, we conducted a comprehensive sensitivity analysis via the following five strategies [28] (for details, see Methods and Supplementary Fig 19-24): i) To minimize the influence of head motion, we replicated the main analysis via data from 24,494 participants with a stricter motion threshold (mFD < 0.2 mm). ii) To assess the potential effects of sampling, we performed 1,000 bootstrap resampling iterations. iii) To evaluate the reproducibility of our results, we implemented a split-half replication strategy. iv) To examine the potential influence of specific sites, we performed leave-one-site-out analyses. v) To address biases from unbalanced sample sizes and site distributions across age groups, we employed a balanced resampling approach (1,000 times). The results of these sensitivity analyses were statistically compared with the main results. At the global and system levels, all the growth curves strongly correlated with the main results (global measures: Pearson's r =0.99±0.01, MSE=$9.5\times10^{-5}\pm1.7\times10^{-4}$; Fig. 6a; system-level measures: Pearson's r =0.98±0.03, MSE=$3.5\times10^{-5}\pm5.5\times10^{-4}$; Fig. 6b). The peak ages of gradient values for each system identified in the validation results closely aligned with those observed in the main results (mean standard deviation age = 0.91 years; Fig. 6c). All sensitivity analyses replicated system-based exclusion results (Fig. 6d and Supplementary Table 6). The regional lifespan growth rate of the S-A gradient was highly consistent across analytical strategies: 95.4% of vertices showed intraclass correlation coefficient values greater than 0.5 and the overall minimum mean square error (MMSE) remained low ($< 5 \times 10^{-6}$) (Fig. 6e). Furthermore, the lifespan growth axis showed strong consistency across strategies ($r = 0.97 \pm 0.01$), with each strategy clearly differentiating the S-A axis (Fig. 6f).

To evaluate the influence of sample size, we conducted a resampling-based sensitivity analysis across sample sizes ranging from 200 to 33,000 participants. Both mean absolute error (MAE) and root mean squared error (RMSE) decreased as sample size increased (Supplementary Fig. 25). Notably, errors at the global and system levels declined sharply until approximately 5,000 participants, after which further reductions plateaued. Regionally, a sample size of ~6,000 participants was required to achieve stable error estimates for more than half of cortical vertices, while a quarter of vertices demanded even larger samples. This analysis indicates that larger samples are essential for reliable gradient growth curves and offers practical guidance for future lifespan neuroimaging studies.

Discussion

Using multimodal MRI, we mapped the spatiotemporal maturation of the S-A gradient across the lifespan. We delineated three distinct developmental phases: initiation, establishment, and expansion and stability. The most pronounced changes occur predominantly during the first decade, with continued refinement extending into mid-adulthood. This gradient maturation proceeds along the S-A axis, aligning with known evolutionary hierarchies, segregation–integration dynamics, structural maturation patterns, and cognitive spectrum. These results establish a unified neurodevelopmental framework linking gradient maturation to multifaceted functional and structural properties.

The lifespan growth of the S-A gradient unfolds in three distinct phases, reflecting developmental milestones of the cortical functional hierarchy. During the perinatal period, functional architecture begins organizing along gradients, with an initial anterior-posterior

differentiation, consistent with prior findings in preterm, term-born, and neonatal cohorts [18,19]. At this early stage, primary regions undergo substantial modifications, resulting in increased functional differentiation and segregation [38]. These changes are likely driven by early survival demands related to vision, audition, and motor functions [39,40]. In contrast, transmodal systems, such as the DMN and FPN, remain sparsely connected, particularly between their anterior and posterior components [38,41]. These connectivity patterns align with known development of neurogenesis, synaptogenesis, and myelination, which follow a rostro-caudal axis [42]. The neuroaxis constitutes a fundamental principle of early cortical organization, providing the structural foundation for the progressive reorganization of functional circuits. Notably, one recent study [23] suggests that the S-A gradient is already present at birth. The discrepancy may partly arise from methodological differences: the previous study [23] applied lifespan generalized additive mixed modeling, which could smooth over less differentiated early-stage patterns.

As the brain progresses into early childhood, the initial anterior–posterior gradient transitions into the more complex S-A gradient. This shift is likely driven by increasing functional specialization and the strengthening of long-range connectivity [38,41]. During this period, neural circuits undergo synaptic pruning and selective reinforcement, promoting the segregation of functional systems [43]. The maturation of higher-order networks is characterized by the progressive integration of distant regions during early and late childhood. Specifically, the DMN exhibits a prolonged period of development, gradually increasing its anterior–posterior connectivity while simultaneously segregating from the FPN [44]. This dual process ultimately reinforces the transmodal apex of the cortical hierarchy. In contrast, attentional networks exhibit weaker and more variable alignment with the gradients during this stage. This transient instability is consistent with broader reorganization of cortical functional architecture, and may contribute to the gradual emergence and consolidation of the S-A gradient in subsequent stages. From late childhood through adolescence into adulthood, the S-A gradient undergoes continued expansion and refinement. This period is marked by increased gradient range and variance, reflecting ongoing network differentiation. Expansion is most pronounced within association cortices, which continue to develop and reorganize, whereas primary regions remain relatively stable. Notably, our definition of Phase III (5-80 years) reflects the prolonged refinement and stabilization of the S-A gradient from childhood, adolescence to adulthood, rather than developmental uniformity through this period.

Across the lifespan, the development of the S-A gradient is tightly coupled with changes in topologic organization. Local segregation, measured by clustering coefficient and within-system FC, followed a coherent trajectory from primary to association cortices. In contrast, functional integration, assessed via regional efficiency and between-system FC, exhibited more regionally specific effects and less continuous alignment with the S-A gradient. These findings are consistent with prior work indicating that functional maturation broadly follows the S-A axis [2]. For instance, Pines et al. demonstrated that between-network coupling matures along this hierarchy during youth [35], and Luo et al. reported strong associations between both segregation and integration trajectories and the S-A axis [36]. Our results extended these previous studies by demonstrating that segregation provides a stable scaffold facilitating hierarchical cortical progression, while integration selectively expands the dynamic range and flexibility of the cortical hierarchy (Supplementary Fig. 26), particularly during periods of heightened cross-system coordination and network reorganization (Supplementary Fig. 27).

The spatial distribution of cortical thickness and intracortical myelination closely parallels functional differentiation throughout the lifespan, following a gradual transition from sensorimotor to association regions. Sensorimotor areas are usually characterized by high neuronal density and well-defined cortical layers, whereas association cortices exhibit lower neuronal density and more diffuse laminar organization [45]. Moreover, primary regions are uniformly myelinated across all cortical layers, whereas association areas are lightly myelinated in superficial cortical layers [8]. This differentiation in laminar architecture lays the foundation for functional differentiation. The "architectonic type principle" suggests that cortical connectivity is shaped by the degree of cytoarchitectonic differentiation [45]. According to this principle, lower-order cortical areas, which are dominated by feedforward projections, originate mainly from supragranular layers. In contrast, higher-order association areas involve feedback processing rely more on infragranular projections [46]. These layer-specific structural properties give rise to distinct intrinsic circuits that shape functional connectivity along the S-A axis. Thus, the hierarchical organization of the cortical macrostructure and microstructure serves as a fundamental scaffold for functional network organization, shaping the connectivity differentiation across the S-A axis.

Our findings revealed a unified lifespan growth S-A axis embedded within a multifaceted neurobiological framework, incorporating the functional connectome, functional segregation, cortical cytoarchitecture, and area expansion, all of which align with the cortical evolutionary hierarchy (Supplementary Fig. 28). This axis reflects a neurodevelopmental hierarchy that captures the temporal sequence of brain development, progressing from primary to transmodal association cortices [2]. Within this framework, functional segregation and integration mature along the S-A axis. Primary networks initially exhibit segregation due to enhanced short-range within-system connections, supporting local specialization [38]. As development advances, the integration of primary and association cortices follows distinct trajectories, likely driven by enhanced long-range connections and the weakening of short-range connections [44]. Complementing these functional changes, cortical thickness undergoes regionally heterogeneous changes. Primary and unimodal cortices exhibit early and rapid thinning, whereas association regions follow a more protracted trajectory. Similarly, surface area expansion aligns with this pattern, with primary and association cortices displaying distinct growth trajectories (Supplementary Fig. 29), reflecting the spatiotemporal dynamics of cortical folding and complexity [30]. The convergence of these multifaceted neurobiological growth patterns suggests the existence of a widely conserved principle governing cortical development, likely shaped by evolutionary constraints. This unified axis reflects an efficient developmental strategy in which phylogenetically older primary sensorimotor systems stabilize early to support basic functions, whereas evolutionarily newer association regions undergo prolonged refinement to accommodate higher-order cognition [47,48]. The decoupling of intracortical T1w/T2w contrast ratio from this axis may stem from different developmental trajectories between sensorimotor and paralimbic regions. Sensorimotor regions exhibit early maturation in microstructural properties such as myelination, whereas paralimbic areas demonstrate prolonged plasticity with myelination and synaptic pruning continuing into adulthood [49]. Notably, while the T1w/T2w ratio is frequently used as a proxy for cortical myelin, it is not specific to myelin, but reflects a composite of microstructural factors (e.g., myelin, iron content, and water concentration) influencing T1 and T2 relaxation times [10,50]. This limitation is pronounced during infancy, where high water content, low iron concentration, and immature myelination reduce its specificity as a microstructural marker, potentially obscuring structure–function coupling.

Our study reveals a dynamic alignment between functional gradient maturation and the canonical cognitive architecture of adulthood. Our objective was not to chart the emergence of cognitive functions in early life, but to examine the extent to which age-specific functional gradients converge toward this mature cognitive architecture. Within this interpretive scope, the observed developmental narrowing of gradient bin widths signifies a progressive refinement of functional organization toward adult-like specialization. This convergence likely reflects the maturation of cortical systems that, in adulthood, become preferentially engaged in distinct cognitive processes, rather than tracking the direct development of cognition per se. Early development is characterized by a more diffuse functional organization, whereas later development shows increased network segregation along the S-A axis, consistent with prior work highlighting an early prioritization of network differentiation [38,44]. This refinement serves to compartmentalize basic perceptual-motor functions and abstract cognition [34,38]. By adolescence, the relative stabilization of gradient bin widths suggests a consolidation of this adult-like functional topography. Notably, cognitive-gradient correspondence continues to strengthen into early adulthood. Ultimately, the S-A gradient constitutes a neurodevelopmental scaffold that bridges the maturation of brain networks with the organization of the cognitive spectrum. Its lifespan pattern suggests that age-related changes in cognitive organization are not merely a product of skill accumulation but are paralleled by a progressive reconfiguration of cortical hierarchy. These insights establish the S-A axis as a central framework for understanding how neurobiological development and cognitive growth are interrelated across the lifespan.

We observed sex differences in the maturation of the S-A gradient across the lifespan. Females exhibited higher gradient magnitudes than males, particularly within transmodal association cortices. This finding aligns with prior work demonstrating that sex differences in functional topography are most prominent in association networks [51], and that these systems also show the greatest interindividual variability in cortical organization [52,53]. The elevated sensorimotor-association differentiation in females likely reflects more pronounced functional segregation within higher-order networks [54]. Notably, these transmodal systems reach peak gradient maturation later in females than in males, suggesting that their heightened functional differentiation may arise from a protracted developmental trajectory. These differences in maturational timing offer a potential neurobiological view for understanding sex disparities in the prevalence and manifestation of neurodevelopmental and psychiatric conditions during adolescence, a period marked by substantial reorganization of hierarchical network architecture.

Several limitations should be noted. First, the uneven distribution of participants across age groups, particularly the underrepresentation of infants and older adults, may restrict our ability to capture the nuances of S-A gradient growth throughout the entire lifespan. While we validated our main findings via rigorous age- and site- matching data, future studies should prioritize collecting high-quality imaging data from these underrepresented populations to achieve a more balanced sampling. Second, the dataset disproportionately includes populations from Europe, North America, Asia and Australia, which limits the result generalizability. Future studies should include participants from a broader range of cultural and socioeconomic backgrounds. Third, the cross-sectional design of this study cannot fully capture the age-related changes in the functional gradient, potentially underestimating the trajectories [55]. Future studies should prioritize the collection of longitudinal data, tracking individuals across multiple time points. Fourth, our cognitive-gradient analysis relied on an adult-derived cognitive reference map, which inherently lacks cognitive development. Future research is important for elucidating cognition-gradient

association across lifespan. Fifth, while all fMRI data were processed with a unified analysis pipeline, cortical surface reconstruction employed age-specific tools. Therefore, we cannot exclude the possibility that methodological differences in surface reconstruction introduced systematic variance into the structural gradient estimation. A fundamental technique challenge is that no neuroimaging framework can robustly process structural data across the entire lifespan. Although the foundation model approach [56] represent promising steps toward integration, the future development of harmonized, lifespan-applicable tools will be essential to overcome this limitation. Finally, the acquisition states differed across the developmental stages of our fMRI sample: neonate and infant data were primarily acquired during natural sleep, whereas children and adults were scanned during wakefulness. Given that functional brain organization (e.g., DMN) differs between sleep and wakefulness [57], this variation in scanning conditions represents a potential confound when estimating the gradient development. This is particularly relevant for Phase II of our analysis, which spans both infancy and childhood. Future studies using standardized scanning protocols will be important to clarify this ambiguity.

Methods

Data acquisition, quality control, and preprocessing

In this study, we collected 3T structural and task-free functional MRI data, comprising 44,576 imaging scans from 42,428 participants ranging in age from 32 PMW to 80 years across 172 distinct sites. For participants with multiple imaging sessions, only the first scan was selected for inclusion, ensuring that each individual contributed a single observation to the analyses. Each dataset received approval from its respective local ethics committee, and written informed consent was obtained from all participants or their legal guardians. The detailed participant demographics and imaging scan parameters can be found in our prior work [28]. To ensure the accuracy and reliability of the neuroimaging data, we implemented a rigorous multistep quality control (QC) framework that combines automated assessments and expert manual inspections (https://github.com/sunlianglong/BrainChart-FC-Lifespan/blob/main/QC/README.md). The final dataset comprised 33,247 participants aged between 32 PMW and 80 years with cross-sectional high-quality structural and functional MRI from 132 sites. The structural MRIs were preprocessed via cortical surface-based processing pipelines [58–60], including skull stripping, tissue segmentation, cortical reconstruction, and cortical surface measurement calculation. The functional MRIs were initially preprocessed in volumetric space with slice timing, motion correction, echo planar imaging (EPI) distortion correction, registration to anatomical images, intensity normalization, and subsequently in surface space with linear trend removal, nuisance regression, temporal bandpass filtering, scrubbing, surface-based smoothing, and resampling to fsaverage4 space (2562 vertices for each hemisphere). More detailed QC and preprocessing procedures can be found in our prior study [28].

Connectome gradient analysis

Following functional MRI preprocessing, we computed pairwise Pearson's correlations between the timeseries of each vertex pair in fsaverage4 (excluding the medial wall) to generate a 4609 × 4609 functional connectome matrix for each participant [28]. The functional connectome matrices underwent Fisher r-to-z transformation to enhance the normal distribution of correlation coefficients.

We first investigated how the S-A axis is established during early development and when it becomes a canonical gradient of cortical functional organization at the group level. Given that functional gradients can be influenced by scanning parameters [61], we selected several major datasets, including the Developing Human Connectome Project (dHCP), Baby Connectome Project (BCP), Children Brain Development Project (CBDP), Human Connectome Project-Development (HCP-D), Human Connectome Project-Young (HCP-Y), and Human Connectome Project-aging (HCP-A), that cover the entire age range and share similar scanning parameters, such as similar spatial and temporal resolutions, and longer scan durations, which are preferable for obtaining reliable functional gradients (the age range covered by each dataset and scanning parameters are shown in Supplementary Table 7). Among the datasets meeting these criteria, the selected datasets also have the largest sample sizes within their corresponding age groups. The participants from these datasets were divided into 26 distinct age groups with finer intervals during the early years and broader intervals during adulthood. To calculate the group-level mean functional connectome, individual connectivity matrices were weighted using Gaussian distribution probability values corresponding to the ages within each group. The group mean connectome for each age group was then computed by averaging the weighted connectivity matrices, with normalization by the sum of the Gaussian weights. The age-specific group mean connectomes were then converted back to r-values via a hyperbolic tangent function, ensuring scaling between -1 and 1.

We identified cortical functional connectome gradients via the BrainSpace toolbox (https://github.com/MICA-MNI/BrainSpace) [62]. To enhance the reliability of gradient estimation while preserving meaningful individual variability, we applied a row-wise top 10% threshold to each group mean connectome, retaining the strongest connections for subsequent gradient analysis [61]. This method was validated by repeating the analyses with a stricter top 5% threshold, which yielded highly consistent results (Supplementary Fig. 30). We subsequently computed the row-wise cosine similarity to generate the affinity matrix, which represents the similarity of the vertex-wise functional connectivity profiles (Supplementary Fig. 31). The well-validated diffusion map embedding [3,25] was applied to identify principal eigenvectors, known as functional gradients, which explain spatial variations in functional connectivity. Applying this algorithm to the affinity matrix allows us to identify multiple low-dimensional gradients that explain the variance in functional connectivity in descending order. For each eigenvector, a value was assigned to each cortical vertex, yielding a cortical map reflecting the gradient topography and visualizing macroscale continuous transitions in overall connectivity patterns. The diffusion embedding is controlled by a single parameter α, which influences the density of sampling points on the underlying manifold. On the basis of prior work, we set $\alpha = 0.5$, which is well suited for brain connectivity data analysis [3].

To ensure accurate comparisons between groups, we applied Procrustes rotation [62] to align age-specific group-level functional gradients to iterative group-level reference gradients. Initially, all group-level functional gradients were aligned to reference gradients obtained from young adults (aged 23-35 years, n = 897) in the Human Connectome Project dataset [37]. We then averaged the aligned gradients of all the groups to obtain new reference gradients. Subsequent alignment iterations refined these reference gradients by aligning all group-level gradients to the new reference gradients, repeating this process 10 times. The final aligned gradients resulted from a combination of the original gradients. We identified the correspondence between the original gradients and the aligned ones on the basis of the largest values of the final transformation

matrices [14]. Compared with constructing the template directly from individual gradients, this multi-step alignment strategy reduces biases from sample size imbalances and development variations in gradient topography.

Individual gradients were computed from each participant's functional connectome using the same procedure and aligned with their corresponding age-specific group-level gradients, which were iteratively aligned to the reference gradient as described above. Following Procrustes alignment, we observed a high spatial correspondence between group-level gradients aligned using different template construction strategies, indicating that the core large-scale topography of the S-A gradient was preserved across alignment procedures (Supplementary Fig. 32a). At the individual level, cosine similarity analyses revealed highly comparable lifespan trajectories across all template choices (Supplementary Fig. 32b), demonstrating that the broad developmental pattern of increasing alignment toward an adult-like S-A organization is robust to reasonable variations in template selection. Within this interpretive framework, template-based similarity metrics primarily reflect alignment to a reference framework rather than independent evidence of biological invariance. In line with recent developmental and comparative gradient studies, we applied no scaling during alignment to retain biologically meaningful differences in gradient range across individuals and age groups. Notably, applying scaling substantially attenuated the developmental trajectory of gradient range (Supplementary Fig. 33), despite maintaining high spatial correspondence (average Spearman's $\rho = 0.99$).

Our subsequent analyses focused on the S-A gradient, given its central role in cortical hierarchical organization encompassing cognition [3], development [19–21,29], disease [13–17], and evolution [30,31].

Identifying distinct growth stages of the S-A gradient axis

To elucidate the temporal sequence of the S-A gradient development, we categorized the age-specific group-level functional gradients into different stages. We first computed the similarity between any two age-specific group-level gradients via cosine correlation coefficients. The similarity matrix was then transformed into a dissimilarity matrix by subtracting the correlation values from 1. Classical multidimensional scaling was applied to reduce the dimensionality of the dissimilarity matrix to two dimensions, explaining 87.9% of the variance in total. This step simplifies the data while preserving its dissimilarity structure, making it more suitable for clustering. We then performed K-means clustering on the two-dimensional dissimilarity matrix to define clusters (phases) of functional gradients from all age groups. The number of clusters was evaluated from 1 to 10, and the optimal number of clusters was determined via a winner-take-all approach on the basis of thirty indices via the NbClust package [63].

Characterizing the growth pattern of the S-A gradient axis

To quantify age-related changes in functional connectome gradients, we comprehensively calculated measures at the global, system and regional levels. At the global level, we computed the explanation ratio, range, and standard deviation for each individual functional gradient. The explanation ratio reflects the percentage of variance in the functional connectivity profile explained by the gradient. The gradient range measures the difference between the two extremes of the gradient with a larger range indicating a greater difference in functional profiles between vertices at the extremes of the gradient. The standard deviation of the functional gradients

represents the heterogeneity of functional connectivity profiles across the cortex. The lifespan growth curves of these measures were fitted via the GAMLSS (for a detailed description, see **Modelling growth curves across the lifespan** section).

At the system level, we used the well-validated age-specific Yeo 7-network atlas to assign cortical vertices to functional systems [28,32,33]. We calculated the gradient range, standard deviation, and gradient values for each functional system and each individual. We then constructed the growth curves of these system-level measures across the lifespan via the GAMLSS. To describe the distribution of gradient values across functional systems along the S-A axis, we performed a descriptive exclusion analysis in which vertices belong to individual system were removed from the precomputed gradients and the resulting changes in mean gradient values were quantified (Δ mean gradient value) for each individual. The Δ mean gradient value for each system was normalized by vertex number of that system. We then performed repeated-measures -ANOVA on the Δ mean gradient value to assess variations in system contribution across different developmental phases. In this analysis, the functional system was regarded as a within-subject factor, and the developmental phase was regarded as a between-subject factor. Interaction effects between the functional system and developmental phase indicate whether the development of the Δ mean gradient value differs among functional systems. The main effects of the functional system revealed variation in the Δ mean gradient value across different systems. The main effects of developmental phase indicate overall changes in the Δ mean gradient value across different phases. Post-hoc pairwise t-test comparisons with Bonferroni correction were performed to examine specific differences between functional systems and phases. All statistical tests were two-sided.

We then investigated the spatiotemporal growth patterns of the functional gradients at the regional level. We first fitted the growth curves of the functional gradient for each vertex via GAMLSS, and computed the first derivative to estimate the growth rate. Next, to identify the spatial axis that explained the largest variance in the age-related changes in gradient values across the cortex, we applied data-driven PCA to the fitted growth curves of functional gradient across all vertices. The first PC is referred to as the principal lifespan growth axis, capturing variability in lifespan growth profiles within a low-dimensional representation. To characterize the variation in growth curves and growth rate curves along this principal lifespan growth axis, we divided the axis into 20 decile bins and calculated the average gradient values and growth rates for all vertices within each bin. To explore the relationships between this lifespan growth axis and other neurobiological properties, we computed Spearman's correlation coefficients between the principal lifespan growth axis and the S-A axis derived from the functional connectome of HCP young adults. To evaluate potential nonlinearity in spatial correlation analyses, we compared first-order (linear) and second-order (quadratic) models using Akaike Information Criterion (AIC)-based model selection. A quadratic term was retained only when it yielded a ≥5% reduction in AIC relative to the linear model, otherwise linear models were retained. Model order was limited to second order to balance flexibility and interpretability. Additionally, we assessed the correlation between the lifespan growth axis and the cortical evolutionary hierarchy, which was quantified by mapping macaque-to-human cortical expansion [30]. This cortical evolutionary hierarchy was obtained from the neuromaps dataset [64] and downsampled to the fsaverage4 space via the neuromaps toolbox (https://github.com/netneurolab/neuromaps). The significance of these correlation analyses were determined using non-parametric 1,000 spin permutation tests that control for spatial

autocorrelations [65].

Modelling growth curves of the S-A gradient axis

We used the Generalized Additive Models for Location, Scale, and Shape (GAMLSS) model to estimate age-related changes in functional gradients across the lifespan from 33,247 functional MRI scans. GAMLSS is a flexible statistical framework that models not only the mean of a brain phenotype but also its variability and distribution shape [26]. The model was optimized to estimate nonlinear lifespan growth curves, their confidence intervals, and the first derivatives of these curves. The reliability of the models was assessed via several sensitivity analysis procedures, including bootstrap resampling, leave-one-site-out, balanced resampling, and split-half replication procedures (see the **Sensitivity analyses** section).

i) Distribution selection

We employed the *gamlss* package (version 5.0-6) in R to establish growth curves for each global, system-level and regional measure. The process begins by evaluating a range of three- or four-parameter GAMLSS distribution families to identify the best-fitting distribution, with GAMLSS fitted to global brain phenotypes, including the explanation ratio, gradient range, and standard deviation for each distribution type. The selection process started with fitting a baseline normal distribution model, which served as a reference. We then systematically evaluated a broad range of potential distributions via the *chooseDist* function, which ranks distributions on the basis of the Bayesian Information Criterion (BIC). The optimal distribution was selected as the one with the lowest BIC.

We found that while the optimal model varied across different brain phenotypes, the skew exponential power type 4 (SEP4) distribution generally yielded the lowest BIC compared with that of other distribution families (Supplementary Fig. 34). Thus, we used the SEP4 distribution in GAMLSS to estimate the age-related changes in functional gradients, with age, sex, mFD and site as predictors. To align the dHCP dataset with other cohorts, we converted gestational age to chronological age. The conversion was based on the assumption that 40 gestational weeks corresponds to birth (0 years of chronological age). The specific formula applied was: Chronological age (years) = (Gestational age at scan – 40) × 7 / 365. This procedure ensured all ages were referenced to a consistent postnatal timeline.

ii) Model fitting

SEP4 is a four-parameter distribution: median (μ), coefficient of variation (σ), skewness (ν) and kurtosis (τ). The parameters were specified as follows: The location parameter (μ) included age as a smoothing term, sex and mFD as fixed effects, and site as a random effect. The scale parameter (σ) included age as a smoothing term, and sex as a fixed effect. The skewness (υ) and kurtosis (τ) parameters were fixed at 1. The model equation is as follows:

$$y = SEP4(\mu, \sigma, \nu, \tau) \quad (1)$$

$$\mu = f_{\mu}(age) + \beta_{\mu}^{1}(sex) + \beta_{\mu}^{2}(mFD) + z_{\mu}(site) \quad (2)$$

$$\sigma = f_{\sigma}(age) + \beta_{\sigma}(sex) \quad (3)$$

$$\nu = \beta_{\nu} \quad (4)$$

$$\tau = \beta_\tau \quad (5)$$

Considering the complexity of lifespan growth trends, we explored a range of model parameters to capture age-related changes. Specifically, we fitted three models with varying degrees of freedom for the age spline in the location parameter: 3, 4, or 5 degrees of freedom. The degree of freedom for the age spline in the scale parameter was set to 3. The convergence criterion was set to a default log-likelihood value of 0.001 between iterations, with a maximum of 200 iteration cycles. The best-fitting model was selected on the basis of having the lowest BIC value.

Once the optimal model was selected, we used it to generate predictions and compute the median growth curve, along with the model parameters (μ, σ, ν, and τ). These parameters were then used to calculate quantiles. To explore sex-specific growth curves, quantile curves for ages ranging from 32 PMW to 80 years were generated separately for males and females across different sites. For each site and sex combination, we computed quantiles at the 0.05, 0.25, 0.5, 0.75, and 0.95 percentiles, resulting in age-specific growth curves.

iii) Model evaluation

To comprehensively evaluate the fit of our GAMLSS, we employed a combination of residual analysis and predictive performance metrics. We first analyzed normalized quantile residuals, which are recommended for GAMLSS diagnostics because of their suitability for complex distributional models. Specifically, we examined residuals plots against the fitted values of the location parameter (μ), residuals against observation indices, kernel density estimation of residuals and the normal quantile−quantile (Q−Q). Our results revealed a well-behaved residual pattern (Supplementary Fig. 35), with residuals distributed uniformly around the horizontal zero line in the residuals versus fitted values or observation indices plots. Kernel density plots suggested indicating an approximately normal distribution, and Q–Q plot displayed a straight-line relationship with a near-zero intercept and a slope close to one. The detrended transformed Owen's plots confirmed that residuals remained within the nonparametric confidence intervals (Supplementary Fig. 36). These diagnostic results indicate that the GAMLSS provided an adequate fit, with residual patterns supporting the assumption of normality and no evident systematic deviations.

To complement the residual diagnostics and evaluate the predictive accuracy, we conducted a cross-validation procedure by dividing the dataset into training and testing sets. We split all the participants into two groups, balanced for age and site. The two groups consisted of 16,661 and 16,586 participants respectively. We computed the R-squared (R^2) values to quantify the explained variance in the central tendency in the testing set. Furthermore, centile calibration was evaluated via randomized z-scores, with normality assessed via the Shapiro–Wilk test. A W statistic close to 1 indicated a good fit. We also examined skewness and kurtosis to measure distribution symmetry and tail behavior. A skewness near zero reflected a symmetric distribution, whereas a kurtosis close to zero indicated well-behaved residual distributions without heavy tails (Supplementary Fig. 37 and Supplementary Table 8).

Relating network segregation/integration to the S-A gradient axis

The segregation and integration of the functional connectome reflect local information specialization and global information integrity within the brain network, respectively [34]. In our prior work, we demonstrated that functional segregation and integration mediate the

development of global S-A gradient metrics in children [20]. Here, we aimed to investigate whether the maturation of the S-A gradient is coupled with the development of functional segregation and integration across the lifespan. We first applied a 10% density threshold to each individual's functional connectivity matrix and binarized the network. We then computed graph theoretical metrics via our Parallel Graph-theoretical Analysis (PAGANI) toolbox [66] (https://www.nitrc.org/projects/pagani_toolkit/) to evaluate functional segregation and integration. For each node, we calculated the clustering coefficient ($C_{p\text{-}node}$) and path length ($1/L_{p\text{-}node}$). The clustering coefficient is the fraction of triangles around a node and quantifies the local clustering and closeness of a network. The path length is the average shortest path length from a given node to all other nodes, providing a measure of network integration and global routing efficiency. The global C_p and $1/L_p$ were derived by averaging these metrics across all nodes. To mitigate potential issues caused by extreme path lengths, we used the inverse of the path length to ensure more accurate model estimation by reducing the influence of outliers. To verify the robustness of the findings, we additionally performed weighted network analyses (Supplementary Fig. 38).

The GAMLSS was applied to fit the lifespan growth trajectories of the global and regional measures. After obtaining the growth curves for the $C_{p\text{-}node}$ and $1/L_{p\text{-}node}$ at each vertex, we computed Spearman's correlation coefficients between the fitted cortex-wide S-A gradient maps and the fitted $C_{p\text{-}node}$ and $1/L_{p\text{-}node}$ maps at the corresponding ages. This approach allowed us to examine the growth pattern of the spatial correspondence between the S-A gradient and functional segregation/integration across the lifespan. In addition, we performed PCA on the fitted growth profiles of $C_{p\text{-}node}$ and $1/L_{p\text{-}node}$ to identify the principal lifespan growth axis for both segregation and integration. We then assessed the correlation between the lifespan growth axis of the S-A gradient and the lifespan growth axes of segregation and integration, respectively. Statistical significance was determined via 1,000 non-parametric spin tests that control for spatial autocorrelations [65]. All *p*-values of the spatial correlation between the S-A gradient and functional segregation/integration were corrected with multiple comparisons controlling for a false discovery rate (FDR) [67] of less than 0.05.

Relating structural and geometric hierarchies to the S-A gradient axis

To explore the structural basis of functional organization across the human lifespan, we assessed the spatial correlation between the S-A gradient and various multifaceted structural attributes, including: i) the geometric distance, defined as the shortest path between two vertices along the cortical surface, reflecting intrinsic cortical geometry [3,24]; ii) macrostructural cortical thickness, representing the distance between white matter and pial surfaces, which correlates with cortical cytoarchitecture [7]; and iii) intracortical T1w/T2w contrast ratio, derived from the signal intensity ratio of T1-T2-weigthted images, providing an indirect measure of regional myeloarchitecture [9].

i) Geometric distance

Considering the geometric constraints on the functional dynamics [24] and spatial arrangement [3], we explored whether the lifespan growth of the S-A gradient correlates with changes in the macroscale geometry. We analyzed the lifespan changes of the geometric distance and its correlation with the S-A gradient. We considered only vertices with top and bottom 5% S-A gradient values because their differences are indicative of cortical functional differentiation and computational constraints. The geometric distance between any two vertices is computed as the

shortest path between them on the triangle surface mesh via the *wb_command -surface-geodesic-distance* implemented in the workbench command (https://www.humanconnectome.org/software/workbench-command/-surface-geodesic-distance). We computed the geometric distance on the mid-thickness surface in the fsaverage_LR32k native space. To account for inter-individual differences in brain size, geodesic distances were normalized by the square root of the cortical surface area. We then obtained the geometric distance matrix between the paired top and bottom gradient vertices. The growth curve and its growth rate curve for the mean geodesic distance were charted via GAMLSS to evaluate the lifespan changes in the geometry between most functionally differentiated regions. Then, the cosine similarity between paired geometric distances and gradient value differences was computed to measure the correlation between the geometric distance and S-A gradient. The growth curve and its growth rate curve for the cosine similarity were charted via GAMLSS to evaluate the lifespan changes in the geometric constraints on functional differentiation.

ii) Cortical thickness

Cortical thickness is one of the most commonly used cortical morphological measures and is related to cortical cytoarchitecture [7]. We aimed to investigate how lifespan changes in cortical thickness are related to the increase in functional differentiation, as indicated by the S-A gradient across the lifespan. The cortical thickness computation was implemented in the HCP structural preprocessing pipeline [60]. The cortical thickness was computed between the white (gray–white interface) and pial surfaces in native space. For each vertex, the shortest distance of that vertex to any other vertex on the other surface was found. The shortest distances from the pial to the white surface and from the white to the pial surface were then averaged to compute the cortical thickness. The cortical thickness for each participant was resampled from native space to fsaverage_LR32k space and then to fsavareage4 space. The final cortical thickness data were derived from 24,992 extensive scans collected from 77 sites. The age and site distributions can be found in Supplementary Fig. 39a.

iii) Intracortical T1w/T2w contrast ratio

Intracortical myelination, a key marker of brain plasticity, develops in stages and different regions across the lifespan with primary motor and sensory regions reaching all milestones earlier than association regions do [49]. We explored the impact of intracortical myelination growth on functional S-A gradient growth across the human lifespan. Intracortical myelination was assessed via a previously validated T1-weighted (T1w) /T2-weighted (T2w) contrast ratio approach [9,60] and subsequent improvements [68,69]. To mitigate inter-scanner variability and enhance cross-site comparability, all T1w and T2w images underwent bias correction and intensity normalization prior to the computation of the T1w/T2w ratio. We estimated intracortical T1w/T2w contrast ratio within the accurate, high-resolution cortical ribbon volume produced during the preprocessing pipeline. The T1w image was divided by the aligned T2w image within voxels between the white and pial surfaces. The division helps cancel out signal intensity bias related to the sensitivity profile of radio frequency receiver coils, enhancing myelin contrast. This ratio was then mapped onto the mid-thickness surface in fsaverage_LR32k space, which was created by averaging the white and pial surfaces, minimizing partial volume effects. The T1w/T2w ratio maps were resampled to fsaverage4 space. The final intracortical T1w/T2w contrast ratio data were extracted from 18,502 scans from 11 sites. The age and site distribution can be found in Supplementary Fig. 39b.

To quantify the structural substrates of S-A gradient growth, we examined its relationship with morphometric (cortical thickness) and microstructural metrics (T1w/T2w contrast ratio). First, we fitted the growth curves of the structural attributes for each vertex via GAMLSS with age and sex as fixed effects, and site as a random effect. We obtained the fitted structural attribute maps and their corresponding growth rate maps across the lifespan. We computed the Spearman correlation coefficients between the fitted cortex-wide S-A gradient maps and the fitted structural attribute maps at corresponding ages. We obtained the growth curve of the spatial correspondence between the gradient and structural attributes across the lifespan. The same PCA analyses were performed on the fitted growth profiles of cortical thickness and intracortical T1w/T2w contrast ratio. We then assessed the correlation between the lifespan growth axis of the S-A gradient and the lifespan growth axes of cortical thickness and intracortical T1w/T2w contrast ratio, respectively. Significance was determined using non-parametric spin tests that control for spatial autocorrelations [65]. All *p*-values of the spatial correlation between the S-A gradient and structural features were corrected, with multiple comparisons controlling the FDR [67] to be less than 0.05.

Mapping the S-A gradient maturation to the adult cognitive spectrum

To investigate how the organization of the cognitive spectrum along the cortical S-A gradient varies across the lifespan, we conducted a functional decoding meta-analysis using both group-based and person-specific S-A gradients derived from the NeuroSynth database (https://neurosynth.org) [27]. First, we created a reference map of the cognitive spectrum along the S-A axis using data from young adults (n=897) in the HCP database [37]. The cortical regions were divided into 20 bins along the S-A axis and projected to the Montreal Neurological Institute (MNI) volume space via the BrainStat toolbox (https://github.com/MICA-MNI/Brainstat). Following the approach outlined by Margulies et al., 2016 [3], we obtained 24 cognitive terms describing the cognitive spectrum, spanning from perception and action to abstract cognition. We computed the associations between each of the 20 regions and each of the term maps respectively. These cognitive terms were ranked by their weighted average position along the gradient, as illustrated in Fig. 5a. Notably, the HCP database was excluded from the following cognitive spectrum analyses.

For the group-based S-A gradients, we computed the cognitive spectrum maps for each of the 26 age-specific groups, following the same procedure used to generate the reference map. For each map, we calculated the width of the distribution of each cognitive term within the gradient bins to measure the degree of clustering of the corresponding brain regions along the S-A axis. Additionally, we computed Spearman's correlation coefficient between the median position of each term in the gradient bin and the gradient percentile, reflecting the covariation between the cognitive and S-A axes. The mean width across terms and Spearman's correlation differences among stages were tested via the non-parametric Kruskal–Wallis test followed by post-hoc pairwise t-test comparisons with Bonferroni multiple comparison correction. All statistical tests were two-sided. To investigate the temporal growth of the organization for each cognitive term, we modelled their growth curves via the GAMLSS. We also fitted the growth curves of the mean width across terms and Spearman's correlation coefficient using the GAMLSS.

To quantify the similarity between each group-based cognitive spectrum map and the reference map, we computed Dice coefficients, with both the S-A and cognitive axes fixed. We also generated person-specific cognitive spectrum maps along the cortical gradients and assessed

their similarity to the reference map via the same procedure. Finally, to characterize changes in the organization of the cognitive spectrum, we fitted a growth curve and its growth rate curve of the Dice coefficient via the GAMLSS.

Sensitivity analysis

Although the GAMLSS provides automated parameter optimization to best fit the included data, covariates, and random effects, we conducted several sensitivity analyses [28] to test the robustness and reliability of the optimized models.

i) Stricter head motion threshold analysis

To reduce the potential influence of head motion on functional MRI data, we applied a more stringent head motion threshold by excluding participants with a mean framewise displacement (FD) greater than 0.2 mm. After applying this stricter threshold, we reanalyzed the lifespan growth curves for our main findings. Specifically, we reran the GAMLSS using data from the 24,494 participants who met the stricter motion criteria for S-A gradient measures at the global, system and regional levels.

ii) Bootstrap resampling analysis

To examine the lifespan growth curves for a broader population and compute the confidence intervals (CIs), we performed 1,000 bootstrap iterations via stratified sampling with replacement. In each iteration, the relative proportions of age and sex within each interval were maintained. The lifespan age range (from 32 PMW to 80 years) was divided into 10 equal intervals. We then fitted 1,000 growth curves and calculated 95% CIs for the median (50^{th} centile) curve of S-A measures at the global, system and regional levels. These CIs were derived by computing the mean and 1.96 times the standard deviation of the growth curves and growth rates across all 1,000 bootstrap iterations.

iii) Split-half replication analysis

To evaluate the replicability of the lifespan growth curves in independent datasets, we implemented a split-half replication strategy. All participants were randomly assigned to two equally sized groups, with stratification by site. The two groups consisted of 16,661 and 16,586 participants, respectively. We estimated lifespan growth curves via the GAMLSS for each group independently.

iv) Leave-one-site-out analysis

To evaluate the robustness and consistency of the lifespan growth curves, we performed leave-one-site-out analyses. For each of the 132 sites, we excluded data from that site and refitted the GAMLSS to the remaining data from the 131 other sites. We compared the median centile curves derived from the remaining sites with those from the full dataset. The 95% CIs were again computed from the mean and 1.96 times the standard deviation of the growth curves and growth rates across all leave-one-site-out iterations.

v) Balanced resampling analysis

To address potential biases due to unbalanced sample sizes and sites across different age groups, we employed a balanced resampling strategy. This approach ensured an equal number of

participants and sites across each age group. The lifespan age range was divided into 16 age bins, each spanning five years. For each bin, the number of participants and sites was determined on the basis of the bin with the fewest participants and sites, excluding the age groups under 5 years and over 70 years. The smallest participant group had 457 participants (in the age bin 35-40 years), and the smallest site group had 23 sites (in the age bin 40-45 years). For each resampling iteration, 457 participants from 23 sites were randomly selected for all age bins, resulting in 6,770 participants per resample. This process was repeated 1,000 times, and the GAMLSS was refitted for all the global and system-level measures. The consistency of the resampling results was evaluated by computing the correlation between the median growth curves from each resampling and the complete dataset. We repeated the above process once and refitted the GAMLSS for all gradient values of cortical surface vertices.

We compared the results of the sensitivity analyses with the main findings. At the global and system levels, we computed Pearson's correlation coefficients and the MSE between the growth curves from the main results and those from the sensitivity analyses. To validate the lifespan growth of the gradient values for the functional systems, we calculated the standard deviation of the peak age across the validation strategies within each system. Additionally, we conducted repeated-measures-ANOVA on the Δ mean gradient value for each validation strategy. At the regional level, we assessed the consistency of the growth rate curves across the validation strategies by calculating the ICC and MMSE. The ICC was determined by comparing the variance between different time points and the variance within each time point across validations. The MMSE score was calculated as the minimal value of the average squared differences between the growth rates from the validation and those from the main results. Finally, for the lifespan growth axis of the S-A gradient, we computed Spearman's correlation coefficient between the main results and sensitivity analyses.

Data availability

The MRI dataset are partly available at the Adolescent Brain Cognitive Development Study (https://nda.nih.gov/), the Autism Brain Imaging Data Exchange Initiative (https://fcon_1000.projects.nitrc.org/indi/abide/), the Alzheimer's Disease Neuroimaging Initiative (https://adni.loni.usc.edu/), the Age_ility Project (https://www.nitrc.org/projects/age-ility), the Baby Connectome Project (https://nda.nih.gov/), the Brain Genomics Superstruct Project (https://doi.org/10.7910/DVN/25833), the Calgary Preschool MRI Dataset (https://osf.io/axz5r/), the Cambridge Centre for Ageing and Neuroscience Dataset (https://www.cam-can.org/index.php?content=dataset), the Developing Human Connectome Project (http://www.developingconnectome.org/data-release/second-data-release/), the Human Connectome Project (https://www.humanconnectome.org), the Lifespan Human Connectome Project (https://nda.nih.gov/), the Nathan Kline Institute-Rockland Sample Dataset (https://fcon_1000.projects.nitrc.org/indi/pro/nki.html), the Neuroscience in Psychiatry Network Dataset (https://nspn.org.uk/), the Pediatric Imaging, Neurocognition, and Genetics (PING) Data Repository (http://pingstudy.ucsd.edu/), the Pixar Dataset (https://openfmri.org/dataset/ds000228/), the Strategic Research Program for Brain Sciences (SRPBS) MRI Dataset (https://bicr-resource.atr.jp/srpbsopen/), the Southwest University Adult Lifespan Dataset (http://fcon_1000.projects.nitrc.org/indi/retro/sald.html), the Southwest University Longitudinal Imaging Multimodal Brain Data Repository

(http://fcon_1000.projects.nitrc.org/indi/retro/southwestuni_qiu_index.html), and the UK Biobank Brain Imaging Dataset (https://www.ukbiobank.ac.uk/). The dhcpSym surface atlases aged from 32 to 44 postmenstrual weeks is available at https://brain-development.org/brain-atlases/atlases-from-the-dhcp-project/cortical-surface-template/. The UNC 4D infant cortical surface atlases are available at https://www.nitrc.org/projects/infantsurfatlas/. The fs_LR_32k surface atlas is available at https://balsa.wustl.edu/. The NeuroSynth database is available at https://neurosynth.org. All analyses of the Lifespan HCP dataset were conducted in accordance with the NIMH Data Archive (NDA) data use agreement and NIH policies. Source data underlying the main and supplementary analyses are provided with this paper.

Code availability

The codes for this manuscript are available here (https://github.com/QionglingLi/LifespanGradient)[70]. Software packages used in this manuscript include MRIQC v0.15.0 (https://github.com/nipreps/mriqc), QuNex v0.93.2 (https://gitlab.qunex.yale.edu/), HCP pipeline v4.4.0-rc-MOD-e7a6af9 (https://github.com/Washington-University/HCPpipelines/releases), ABCD-HCP pipeline v1 (https://github.com/DCAN-Labs/abcd-hcp-pipeline), dHCP structural pipeline v1 (https://github.com/BioMedIA/dhcp-structural-pipeline), dHCP functional pipeline v1 (https://git.fmrib.ox.ac.uk/seanf/dhcp-neonatal-fmri-pipeline), iBEAT pipeline v1.0.0 (https://github.com/iBEAT-V2/iBEAT-V2.0-Docker), MSM_HOCR v3.0 (https://github.com/ecr05/MSM_HOCR), FreeSurfer v6.0.0 (https://surfer.nmr.mgh.harvard.edu/), FSL v6.0.5 (https://fsl.fmrib.ox.ac.uk/fsl/fslwiki), Connectome Workbench v1.5.0 (https://www.humanconnectome.org/software/connectome-workbench), MATLAB R2020b (https://www.mathworks.com/products/matlab.html), SPM12 toolbox v6470 (https://www.fil.ion.ucl.ac.uk/spm/software/spm12), GRETNA toolbox v2.0.0 (https://www.nitrc.org/projects/gretna), cifti-matlab toolbox v2 (https://github.com/Washington-University/cifti-matlab), GAMLSS package v5.4-3 (https://www.gamlss.com/), Spyder v4.0 (https://www.spyder-ide.org/), Python v3.7 (https://www.python.org), R v4.4.1 (https://www.r-project.org), NbClust package v3.0.1 (https://www.rdocumentation.org/packages/NbClust/versions/3.0.1/topics/NbClust), BrainSpace toolbox v0.1.10 (https://github.com/MICA-MNI/BrainSpace), PAGANI toolbox v1.5 (https://www.nitrc.org/projects/pagani_toolkit/), neuromaps toolbox v0.0.5 (https://github.com/netneurolab/neuromaps), BrainStat toolbox v0.4.2 (https://github.com/MICA-MNI/Brainstat), SurfStat toolbox (https://mica-mni.github.io/surfstat/), plotSurfaceROIBoundary v1.0.1 (https://github.com/StuartJO/plotSurfaceROIBoundary), NeuroSynth meta-analysis code (https://github.com/NeuroanatomyAndConnectivity/gradient_analysis), and the codes for growth modelling, visualization, and sensitivity analyses (https://github.com/sunlianglong/BrainChart-FC-Lifespan/tree/main).

References

1. Huntenburg, J. M., Bazin, P.-L. & Margulies, D. S. Large-Scale Gradients in Human Cortical Organization. *Trends Cogn. Sci.* **22**, 21–31 (2018).
2. Sydnor, V. J. *et al.* Neurodevelopment of the association cortices: Patterns, mechanisms, and implications for psychopathology. *Neuron* **109**, 2820–2846 (2021).
3. Margulies, D. S. *et al.* Situating the default-mode network along a principal gradient of macroscale cortical organization. *Proc. Natl. Acad. Sci.* **113**, 12574–12579 (2016).
4. Mesulam, M. M. From sensation to cognition. *Brain* **121**, 1013–1052 (1998).
5. Aflalo, T. N. & Graziano, M. S. A. Organization of the Macaque Extrastriate Visual Cortex Re-Examined Using the Principle of Spatial Continuity of Function. *J. Neurophysiol.* **105**, 305–320 (2011).
6. Valk, S. L. *et al.* Shaping brain structure: Genetic and phylogenetic axes of macroscale organization of cortical thickness. *Sci. Adv.* **6**, eabb3417 (2020).
7. Fischl, B. & Dale, A. M. Measuring the thickness of the human cerebral cortex from magnetic resonance images. *Proc. Natl. Acad. Sci.* **97**, 11050–11055 (2000).
8. Paquola, C. *et al.* Microstructural and functional gradients are increasingly dissociated in transmodal cortices. *PLOS Biol.* **17**, e3000284 (2019).
9. Glasser, M. F. & Van Essen, D. C. Mapping human cortical areas in vivo based on myelin content as revealed by T1- and T2-weighted MRI. *J. Neurosci.* **31**, 11597–11616 (2011).
10. Baum, G. L. *et al.* Graded variation in T1w/T2w ratio during adolescence: measurement, caveats, and implications for development of cortical myelin. *J. Neurosci.* **42**, 5681–5694 (2022).
11. Burt, J. B. *et al.* Hierarchy of transcriptomic specialization across human cortex captured by structural neuroimaging topography. *Nat. Neurosci.* **21**, 1251–1259 (2018).
12. Dear, R. *et al.* Cortical gene expression architecture links healthy neurodevelopment to the imaging, transcriptomics and genetics of autism and schizophrenia. *Nat. Neurosci.* **27**, 1075–1086 (2024).
13. Hong, S.-J. *et al.* Atypical functional connectome hierarchy in autism. *Nat. Commun.* **10**, 1–13 (2019).
14. Xia, M. *et al.* Connectome gradient dysfunction in major depression and its association with gene expression profiles and treatment outcomes. *Mol. Psychiatry* **27**, 1384–1393 (2022).
15. Hu, Q., Li, Y., Wu, Y., Lin, X. & Zhao, X. Brain network hierarchy reorganization in Alzheimer's disease: A resting-state functional magnetic resonance imaging study. *Hum. Brain Mapp.* **43**, 3498–3507 (2022).
16. Nguyen, T. T. *et al.* Variations in Cortical Functional Gradients Relate to Dimensions of Psychopathology in Preschool Children. *J. Am. Acad. Child Adolesc. Psychiatry* https://doi.org/10.1016/j.jaac.2023.05.029 (2023) doi:10.1016/j.jaac.2023.05.029.
17. He, Y. *et al.* Functional gradients reveal altered functional segregation in patients with amnestic mild cognitive impairment and Alzheimer's disease. *Cereb. Cortex* **33**, 10836–10847 (2023).
18. Larivière, S. *et al.* Multiscale Structure–Function Gradients in the Neonatal Connectome. *Cereb. Cortex* **30**, 47–58 (2020).
19. Xia, Y. *et al.* Development of sensorimotor-visual connectome gradient at birth predicts neurocognitive outcomes at 2 years of age. *Iscience* https://www.cell.com/iscience/pdf/S2589-0042(24)00202-5.pdf (2024).
20. Xia, Y. *et al.* Development of functional connectome gradients during childhood and adolescence. *Sci. Bull.* **67**, 1049–1061 (2022).
21. Dong, H.-M., Margulies, D. S., Zuo, X.-N. & Holmes, A. J. Shifting gradients of macroscale cortical organization mark the transition from childhood to adolescence. *Proc. Natl. Acad. Sci.* **118**, e2024448118 (2021).

22. Bethlehem, R. A. I. *et al.* Dispersion of functional gradients across the adult lifespan. *NeuroImage* **222**, 117299 (2020).
23. Taylor, H. P. *et al.* Functional Hierarchy of the Human Neocortex from Cradle to Grave. Preprint at https://doi.org/10.1101/2024.06.14.599109 (2024).
24. Pang, J. C. *et al.* Geometric constraints on human brain function. *Nature* **618**, 566–574 (2023).
25. Coifman, R. R. *et al.* Geometric diffusions as a tool for harmonic analysis and structure definition of data: Diffusion maps. *Proc. Natl. Acad. Sci.* **102**, 7426–7431 (2005).
26. Stasinopoulos, D. M. & Rigby, R. A. Generalized additive models for location scale and shape (GAMLSS) in R. *J. Stat. Softw.* **23**, 1–46 (2008).
27. Yarkoni, T., Poldrack, R. A., Nichols, T. E., Van Essen, D. C. & Wager, T. D. Large-scale automated synthesis of human functional neuroimaging data. *Nat. Methods* **8**, 665–670 (2011).
28. Sun, L. *et al.* Human lifespan changes in the brain's functional connectome. *Nat. Neurosci.* **28**, 891–901 (2025).
29. Dong, H.-M. *et al.* Ventral attention network connectivity is linked to cortical maturation and cognitive ability in childhood. *Nat. Neurosci.* **27**, 2009–2020 (2024).
30. Hill, J. *et al.* Similar patterns of cortical expansion during human development and evolution. *Proc. Natl. Acad. Sci.* **107**, 13135–13140 (2010).
31. Xu, T. *et al.* Cross-species functional alignment reveals evolutionary hierarchy within the connectome. *NeuroImage* **223**, 117346 (2020).
32. Yeo, B. T. *et al.* The organization of the human cerebral cortex estimated by intrinsic functional connectivity. *J. Neurophysiol.* (2011).
33. Wang, D. *et al.* Parcellating cortical functional networks in individuals. *Nat. Neurosci.* **18**, 1853–1860 (2015).
34. Park, H. J. & Friston, K. Structural and functional brain networks: from connections to cognition. *Science* **342**, 1238411 (2013).
35. Pines, A. R. *et al.* Dissociable multi-scale patterns of development in personalized brain networks. *Nat. Commun.* **13**, 2647 (2022).
36. Luo, A. C. *et al.* Functional connectivity development along the sensorimotor-association axis enhances the cortical hierarchy. *Nat. Commun.* **15**, 3511 (2024).
37. Van Essen, D. C. *et al.* The Human Connectome Project: A data acquisition perspective. *NeuroImage* **62**, 2222–2231 (2012).
38. Li, Q. *et al.* Development of segregation and integration of functional connectomes during the first 1,000 days. *Cell Rep.* **43**, (2024).
39. Gilmore, J. H., Knickmeyer, R. C. & Gao, W. Imaging structural and functional brain development in early childhood. *Nat. Rev. Neurosci.* **19**, 123–137 (2018).
40. Cao, M., Huang, H. & He, Y. Developmental Connectomics from Infancy through Early Childhood. *Trends Neurosci.* **40**, 494–506 (2017).
41. Gao, W. *et al.* Evidence on the emergence of the brain's default network from 2-week-old to 2-year-old healthy pediatric subjects. *Proc. Natl. Acad. Sci.* **106**, 6790–6795 (2009).
42. Cooper, M. L. & Rakic, P. Gradients of cellular maturation and synaptogenesis in the superior colliculus of the fetal rhesus monkey. *J. Comp. Neurol.* **215**, 165–186 (1983).
43. Jacobs, R. A. Computational studies of the development of functionally specialized neural modules. *Trends Cogn. Sci.* **3**, 31–38 (1999).
44. Fair, D. A. *et al.* Functional Brain Networks Develop from a "Local to Distributed" Organization. *PLOS Comput. Biol.* **5**, e1000381 (2009).

45. Hilgetag, C. C., Beul, S. F., van Albada, S. J. & Goulas, A. An architectonic type principle integrates macroscopic cortico-cortical connections with intrinsic cortical circuits of the primate brain. *Netw. Neurosci.* **3**, 905–923 (2019).
46. Felleman, D. J. & Van Essen, D. C. Distributed hierarchical processing in the primate cerebral cortex. *Cereb. Cortex N. Y. NY 1991* **1**, 1–47 (1991).
47. Finlay, B. L. & Darlington, R. B. Linked regularities in the development and evolution of mammalian brains. *Science* **268**, 1578–1584 (1995).
48. Buckner, R. L. & Krienen, F. M. The evolution of distributed association networks in the human brain. *Trends Cogn. Sci.* **17**, 648–665 (2013).
49. Grydeland, H. *et al.* Waves of Maturation and Senescence in Micro-structural MRI Markers of Human Cortical Myelination over the Lifespan. *Cereb. Cortex* **29**, 1369–1381 (2019).
50. Larsen, B. *et al.* Longitudinal development of brain iron is linked to cognition in youth. *J. Neurosci.* **40**, 1810–1818 (2020).
51. Shanmugan, S. *et al.* Sex differences in the functional topography of association networks in youth. *Proc. Natl. Acad. Sci.* **119**, e2110416119 (2022).
52. Cui, Z. *et al.* Individual variation in functional topography of association networks in youth. *Neuron* **106**, 340-353.e8 (2020).
53. Gordon, E. M. *et al.* Precision functional mapping of individual human brains. *Neuron* **95**, 791-807.e7 (2017).
54. Sidhu, A. S. *et al.* Age- and sex-specific patterns in adult brain network segregation. *Hum. Brain Mapp.* **46**, e70169 (2025).
55. Di Biase, M. A. *et al.* Mapping human brain charts cross-sectionally and longitudinally. *Proc. Natl. Acad. Sci.* **120**, e2216798120 (2023).
56. Sun, Y., Wang, L., Li, G., Lin, W. & Wang, L. A foundation model for enhancing magnetic resonance images and downstream segmentation, registration and diagnostic tasks. *Nat. Biomed. Eng.* **9**, 521–538 (2024).
57. El-Baba, M. *et al.* Functional connectivity dynamics slow with descent from wakefulness to sleep. *PloS One* **14**, e0224669 (2019).
58. Wang, L. *et al.* iBEAT V2.0: a multisite-applicable, deep learning-based pipeline for infant cerebral cortical surface reconstruction. *Nat. Protoc.* **18**, 1488–1509 (2023).
59. Makropoulos, A. *et al.* The developing human connectome project: A minimal processing pipeline for neonatal cortical surface reconstruction. *NeuroImage* **173**, 88–112 (2018).
60. Glasser, M. F. *et al.* The minimal preprocessing pipelines for the Human Connectome Project. *Neuroimage* **80**, 105–124 (2013).
61. Hong, S.-J. *et al.* Toward a connectivity gradient-based framework for reproducible biomarker discovery. *NeuroImage* **223**, 117322 (2020).
62. Vos de Wael, R. *et al.* BrainSpace: a toolbox for the analysis of macroscale gradients in neuroimaging and connectomics datasets. *Commun. Biol.* **3**, 1–10 (2020).
63. Charrad, M., Ghazzali, N., Boiteau, V. & Niknafs, A. NbClust: an R package for determining the relevant number of clusters in a data set. *J. Stat. Softw.* **61**, 1–36 (2014).
64. Markello, R. D. *et al.* neuromaps: structural and functional interpretation of brain maps. *Nat. Methods* **19**, 1472–1479 (2022).
65. Alexander-Bloch, A. F. *et al.* On testing for spatial correspondence between maps of human brain structure and function. *NeuroImage* **178**, 540–551 (2018).
66. Du, H. *et al.* PAGANI Toolkit: Parallel graph-theoretical analysis package for brain network big data.

Hum. Brain Mapp. **39**, 1869–1885 (2018).
67. Benjamini, Y. & Hochberg, Y. Controlling the false discovery rate: A practical and powerful approach to multiple testing. *J. R. Stat. Soc. Ser. B Methodol.* **57**, 289–300 (1995).
68. Glasser, M. F., Goyal, M. S., Preuss, T. M., Raichle, M. E. & Van Essen, D. C. Trends and properties of human cerebral cortex: correlations with cortical myelin content. *Neuroimage* **93**, 165–175 (2014).
69. Glasser, M. F. *et al.* Empirical transmit field bias correction of T1w/T2w myelin maps. *NeuroImage* **258**, 119360 (2022).
70. QionglingLi. Spatiotemporal dynamics of the human cortical functional hierarchy across the lifespan, QionglingLi/LifespanGradient: lifespangradient v1. https://doi.org/10.5281/zenodo.18764982 (2026).

Acknowledgments

We thank Lianglong Sun for his valuable contributions to the coordination, quality control, processing of all the imaging datasets, the related analysis code used in this study, and discussion for the main study and validation strategy. This work was supported by grants from the National Natural Science Foundation of China (82021004 and 31830034 to Yong He, 32271146 and 82021004 to S.L, 82071998 to M.X., 82202245 to Q.Li), the scientific and technological innovation 2030 - the major project of the Brain Science and Brain-Inspired Intelligence Technology (2021ZD0200500 to Q.D. and 2022ZD0211500 to M.X.), the Changjiang Scholar Professorship Award (T2015027 to Yong He), the Beijing Natural Science Foundation (JQ23033 to M.X. and 7262077 to T.Z.), the National Key R&D Program of China (2022YFC2009900 to Q. Gong), the National Natural Science Foundation of China (31521063 and 31221003 to Q.D., 824B2051 to X.Liang, T2325006 to G.G., 81971690 to X.Liao, 32130045 and 32361163611 to S.Qin, 81571062 and 82172018 to Yong Liu, 81471120 to X.Z., 61633018 to Y.Han, 81901101 to P.W., 81400890 to D.Wang, 82330058, T2341014, and 81920108019 to S.Qiu, 82430063 to C.Y., 32471096 to J.Q., 82102131 to Y.X., 81425013 to W.Q., and 82027808 to Q. Gong), the Science and Technology Plan Project of Guangzhou (2018-1002-SF-0442 to S.Qiu), the Guangzhou Key Laboratory (09002344 to S.Qiu), and the Key R&D Program of Sichuan Province (2023YFS0076 to T.C.).

We are grateful to the Adolescent Brain Cognitive Development (ABCD) Study, the Autism Brain Imaging Data Exchange (ABIDE) Initiative, the Alzheimer's Disease Neuroimaging Initiative (ADNI), the Age_ility Project, the Baby Connectome Project (BCP), the Brain Genomics Superstruct Project (BGSP), the Calgary Preschool MRI Dataset, the Cambridge Centre for Ageing and Neuroscience (Cam-CAN) Dataset, the developing Human Connectome Project (dHCP), the Human Connectome Project (HCP), the Lifespan Human Connectome Project (HCPA & HCPD), the Nathan Kline Institute-Rockland Sample (NKI-RS) Dataset, the Neuroscience in Psychiatry Network (NSPN) Dataset, the Pixar Dataset, the Southwest University Adult Lifespan Dataset (SALD), the Southwest University Longitudinal Imaging Multimodal (SLIM) Brain Data Repository, the UK Biobank (UKB) Brain Imaging Dataset, the Disease Imaging Data Archiving: major depressive disorder (DIDA-MDD) Working Group, and the Multi-center Alzheimer Disease Imaging (MCADI) Consortium. We thank the National Center for Protein Sciences at Peking University in Beijing, China, for assistance with MRI data acquisition.

ABCD: data used in the preparation of this article were obtained from the Adolescent Brain Cognitive Development (ABCD) Study (https://abcdstudy.org), held in the NIMH Data Archive (NDA). This is a multisite, longitudinal study designed to recruit more than 10,000 children age 9-10 and follow them over 10 years into early adulthood. The ABCD Study® is supported by the National Institutes of Health and additional federal partners under award numbers U01DA041048, U01DA050989, U01DA051016, U01DA041022, U01DA051018, U01DA051037, U01DA050987, U01DA041174, U01DA041106, U01DA041117, U01DA041028, U01DA041134, U01DA050988, U01DA051039, U01DA041156, U01DA041025, U01DA041120, U01DA051038, U01DA041148, U01DA041093, U01DA041089, U24DA041123, U24DA041147. A full list of supporters is available at https://abcdstudy.org/federal-partners.html. A listing of participating sites and a complete listing of the study investigators can be found at https://abcdstudy.org/consortium_members/. ABCD

consortium investigators designed and implemented the study and/or provided data but did not necessarily participate in the analysis or writing of this report. This manuscript reflects the views of the authors and may not reflect the opinions or views of the NIH or ABCD consortium investigators. The ABCD data repository grows and changes over time. The ABCD data used in this report came from https://nda.nih.gov/edit_collection.html?id=3165, shared by the DCAN Labs ABCD-BIDS Community Collection (ABCC) (Collection Investigators: Damien Fair).

ABIDE I: primary support for the work by Adriana Di Martino was provided by the (NIMH K23MH087770) and the Leon Levy Foundation. Primary support for the work by Michael P. Milham and the INDI team was provided by gifts from Joseph P. Healy and the Stavros Niarchos Foundation to the Child Mind Institute, as well as by an NIMH award to MPM (NIMH R03MH096321).

ABIDE II: primary support for the work by Adriana Di Martino and her team was provided by the National Institute of Mental Health (NIMH 5R21MH107045). Primary support for the work by Michael P. Milham and his team provided by the National Institute of Mental Health (NIMH 5R21MH107045); Nathan S. Kline Institute of Psychiatric Research). Additional Support was provided by gifts from Joseph P. Healey, Phyllis Green and Randolph Cowen to the Child Mind Institute.

ADNI: Data used in preparation of this article were obtained from the Alzheimer's Disease Neuroimaging Initiative (ADNI) database (adni.loni.usc.edu). As such, the investigators within the ADNI contributed to the design and implementation of ADNI and/or provided data but did not participate in analysis or writing of this report. A complete listing of ADNI investigators can be found at: http://adni.loni.usc.edu/wp-content/uploads/how_to_apply/ADNI_Acknowledgement_List.pdf. Data collection and sharing for this project was funded by the Alzheimer's Disease Neuroimaging Initiative (ADNI) (National Institutes of Health Grant U01 AG024904) and DOD ADNI (Department of Defense award number W81XWH-12-2-0012). ADNI is funded by the National Institute on Aging, the National Institute of Biomedical Imaging and Bioengineering, and through generous contributions from the following: AbbVie, Alzheimer's Association; Alzheimer's Drug Discovery Foundation; Araclon Biotech; BioClinica, Inc.; Biogen; Bristol-Myers Squibb Company; CereSpir, Inc.; Cogstate; Eisai Inc.; Elan Pharmaceuticals, Inc.; Eli Lilly and Company; EuroImmun; F. Hoffmann-La Roche Ltd and its affiliated company Genentech, Inc.; Fujirebio; GE Healthcare; IXICO Ltd.;Janssen Alzheimer Immunotherapy Research & Development, LLC.; Johnson & Johnson Pharmaceutical Research & Development LLC.; Lumosity; Lundbeck; Merck & Co., Inc.; Meso Scale Diagnostics, LLC.; NeuroRx Research; Neurotrack Technologies; Novartis Pharmaceuticals Corporation; Pfizer Inc.; Piramal Imaging; Servier; Takeda Pharmaceutical Company; and Transition Therapeutics. The Canadian Institutes of Health Research is providing funds to support ADNI clinical sites in Canada. Private sector contributions are facilitated by the Foundation for the National Institutes of Health (www.fnih.org). The grantee organization is the Northern California Institute for Research and Education, and the study is coordinated by the Alzheimer's Therapeutic Research Institute at the University of Southern California. ADNI data are disseminated by the Laboratory for Neuro Imaging at the University of Southern California.

BCP: data used herein is supported by NIH grant (1U01MH110274) and the efforts of the UNC/UMN Baby Connectome Project Consortium.

dHCP: data were provided by the developing Human Connectome Project, KCL-Imperial-Oxford Consortium funded by the European Research Council under the European Union Seventh Framework Programme (FP/2007-2013) / ERC Grant Agreement no. [319456]. We are grateful to the families who generously supported this trial.

HCP: data were provided by the Human Connectome Project, WU-Minn Consortium (Principal Investigators: David Van Essen and Kamil Ugurbil; 1U54MH091657) funded by the 16 NIH Institutes and Centers which support the NIH Blueprint for Neuroscience Research; and by the Mc-Donnell Center for Systems Neuroscience at Washington University.

HCP Lifespan: data used in this publication was supported by the National Institute of Mental Health of the National Institutes of Health under Award Number U01MH109589 and by funds provided by the McDonnell Center for Systems Neuroscience at Washington University in St. Louis. The content is solely the responsibility of the authors and does not necessarily represent the official views of the National Institutes of Health.

NKI-RS: funding for key personnel provided in part by the New York State Office of Mental Health and Research Foundation for Mental Hygiene. Additional project support provided by the NKI Center for Advanced Brain Imaging (CABI), the Brain Research Foundation (Chicago, IL), the Stavros Niarchos Foundation, and NIH grant P50 MH086385-S1.

NSPN: the NSPN study was funded by a Wellcome Trust award to the University of Cambridge and the University College London.

UK Biobank: this research has been conducted using data from UK Biobank (www.ukbiobank.ac.uk). UK Biobank is generously supported by its founding funders the Wellcome Trust and UK Medical Research Council, as well as the Department of Health, Scottish Government, the Northwest Regional Development Agency, British Heart Foundation, and Cancer Research UK.

Author Contributions

Q.Li, M.X., S.L., and Y.He conceptualized the study. Y.He, M.X., and S.L. supervised the project. Q.Li, D.Z., X.Liang, X.D., Y.R.He, T.Z., M.X., S.L., and Y.He designed the methodology. D.Z., X.Liang, and M.X. developed visualizations. D.Z., X.Liao., D.D., Z.Z., Z.X., and Z.C. provided guidance on data analysis and result interpretation. X.Liang, Q.W., C.P., Q.Y., Q.Li., Y.X., R.Huo, H.Y., Ying Liu, and M.X. performed data quality control; G.G., Y.B., P.C., R.C., Y.Chen., T.C., J.C., Y.Cheng, Z.D., Y.Deng, Y.Ding, Q.D., J.H.G., Q.G., Y.Han, Z.H., C.C.H., R.Huang, L.L., C.P.L., Q.Lin, B.L., C.L., N.L., Yong Liu, J.L., L.M., W.M., S.Qin, J.Q., S.Qiu., W.Q., T.S., S.Tan, Y.T., S.Tao, D.Wang, F.W., J.W., P.W., X.W., Y.Wang, D.Wei., Y.Wu., P.X., X.X., C.Y., L.Y., H.Z., X.Z., G.Z., Y.Z., and S.Z. collected a subset of the data for this study. Q.Li, M.X., S.L, and Y.He wrote the manuscript. All authors reviewed the final manuscript.

Competing Interests

The authors declare no competing interests.

Figure Legend

Fig. 1 | Distinct growth stages of the sensorimotor-association gradient across the lifespan. **a**, S-A gradient maps generated for 26 distinct age groups. **b**, K-means clustering analysis based on the pairwise correlations between the 26 group-based gradient maps, resulting in three clusters. **c**, Three distinct phases of the S-A gradient are visualized via multidimensional scaling (MDS). "Dimension 1" and "dimension 2" are defined as the first and second axes obtained through MDS of the functional distance matrix. **d**, Distribution of gradient values in the S-A axis across lifespan. w, week; m, month; yr, year.

Fig. 2 | Lifespan growth of the sensorimotor-association gradient. a, Lifespan growth curves (top panel) and growth rate curves (bottom panel) for global gradient measures. The solid line represents the 50th centile (median), while the dotted lines represent the 5th, 25th, 75th, and 95th centiles. The growth rate was estimated by the first derivative of the median growth curve, with a 95% confidence interval (shaded in gray) obtained from 1,000 bootstrap resamplings. The horizontal dotted line (y=0) marks the transition from growth to decline, with the peak age indicated by a purple dot. **b**, Lifespan growth curves of gradient range and standard deviation for each functional system defined according to the age-specific Yeo 7-network atlas [28,32,33]. **c**, Lifespan growth of the gradient value for each functional system. The peak age is marked by a black dot. **d**, Contributions to lifespan growth of the S-A gradient from each functional system, estimated via descriptive exclusion analysis (left panel). System contributions across developmental phases were assessed using repeated-measures ANOVA, followed by Bonferroni-corrected post-hoc pairwise t-tests. All statistical tests were two-sided. (right panel). ***, $p<0.001$. **e**, Lifespan growth rate maps of the S-A gradient at representative ages. **f**, Lifespan growth axis of the S-A gradient. The left panel shows regional gradient values across age. PCA identified the first component as the dominant lifespan growth axis, explaining 65.4% of the variance (middle panel). The growth axis was divided into 20 decile bins, and mean gradient values were computed for all vertices within each bin (right panel). **g**, Spatial correlation between the lifespan growth axis and the evolutionary hierarchy. Evolutionary hierarchy was quantified using macaque-to-human cortical expansion [30]. Statistical significance was assessed via 1,000 non-parametric spin permutation tests [65]. CI, confidence interval; VIS, visual; SM, somatomotor; DA, dorsal attention; VA, ventral attention; LIM, limbic; FP, frontoparietal; DM, default-mode; w, week; m, month; yr, year.

Fig. 3 | Lifespan growth of functional segregation and integration. a, Lifespan growth and growth rate curves of the global clustering coefficient (C_p), reflecting functional segregation. **b**, Lifespan growth and growth rate curves of the inverse characteristic shortest path length ($1/L_p$), reflecting functional integration. In **a-b**, the solid line represents the 50th centile (median), and the dotted lines represent the 5th, 25th, 75th, and 95th centiles. The growth rate was estimated by the first derivative of the median growth curve, with a 95% confidence interval (shaded in gray) obtained from 1,000 bootstrap resamplings. The horizontal dotted line (y=0) marks the transition from growth to decline or from decline to growth. **c**, Normative growth (top panel) and growth rate (bottom panel) maps of the regional clustering ($C_{p\text{-node}}$) at representative ages. **d**, Normative growth (top panel) and growth rate (bottom panel) maps of regional efficiency ($1/L_{p\text{-node}}$) at representative ages. **e-f**, Lifespan growth axis of functional segregation and integration. The left panel shows regional $C_{p\text{-node}}$ or regional $1/L_{p\text{-node}}$ trajectories across ages. PCA identified the first

component as the dominant lifespan growth axis (middle panel), explaining 74.9% of the variance for regional $C_{p\text{-}node}$ and 57.6% of the variance for regional $1/L_{p\text{-}node}$. The growth axis was divided into 20 decile bins, and mean $C_{p\text{-}node}$ values or mean regional $1/L_{p\text{-}node}$ values were computed for all vertices within each bin (right panel). **g-h**, Spatial correlation between the lifespan growth axis of the S-A gradient and functional segregation/integration. CI, confidence interval; w, week; m, month; yr, year.

Fig. 4 | Lifespan growth of structural hierarchies. a, The two extreme ends of the S-A axis. The boundaries of cortical vertices with the top 5% (black curve) and bottom 5% (orange curve) gradient values are overlaid on the cortical surface. **b**, Lifespan growth and growth rate curves of the mean geometric distance between the two extreme ends of the S-A axis. The solid line represents the 50th centile (median), and the dotted lines represent the 5th, 25th, 75th, and 95th centiles. The growth rate was estimated by the first derivative of the median growth curve, with a 95% confidence interval (shaded in gray) obtained from 1,000 bootstrap resamplings. The horizontal dotted line (y=0) marks the transition from growth to decline, with the peak age indicated by a purple dot. **c**, Lifespan growth and growth rate curves of the coupling between cortical geometry and the S-A axis. **d**, Lifespan growth and growth rate maps of regional cortical thickness at representative ages. **e**, Lifespan growth and growth rate maps of regional intracortical myelination at representative ages. **f**, Lifespan growth axis of cortical thickness. The left panel shows regional thickness trajectories across age. PCA identified the first component as the dominant lifespan growth axis, explaining 97.3% of the variance (middle panel). The growth axis was divided into 20 decile bins, and the mean thickness values were computed for all vertices within each bin (right panel). **g**, Lifespan growth axis of intracortical myelination. PCA identified the first component explaining 89.0% of the variance. **h**, Spatial correlation between the lifespan growth axis of the functional gradient and cortical thickness. **i**, Spatial correlation between the lifespan growth axis of the functional gradient and intracortical myelination. CI, confidence interval; w, week; m, month; yr, year.

Fig. 5 | Lifespan alignment of sensorimotor–association gradient to adult cognitive-functional reference. a, Cognitive spectra at reference (the left) and representative ages over the lifespan. The reference spectrum was generated via a cognitive decoding meta-analysis of the S-A gradient in young adults from the Human Connectome Project (HCP) dataset. The cognitive terms were sorted by their weighted average position along the gradient. **b**, Cognitive term distribution along the S-A gradient across three phases. Illustration of the gradient bin width and the correlation between the term median gradient bin and gradient percentile (left panel). Differences in the mean term width and correlation among the three phases were tested via the non-parametric Kruskal–Wallis test followed by post-hoc pairwise t-test comparisons with Bonferroni multiple comparison correction. All statistical tests were two-sided. In the violin plot, the shape represents the kernel density distribution, dots indicate individual observations, the white dot marks the median, the thick bar denotes the interquartile range, and the thin bar indicate the minimum and maximum values. ***, $p < 0.001$; ** $p < 0.01$; * $p < 0.05$ (middle and right panels). **c**, Lifespan growth and growth rate curves of the cognitive term distribution along the S-A gradient. **d**, Dice coefficients between the group-based cognitive spectrum maps and the reference spectrum across 26 age groups. **e**, Lifespan growth and growth rate curves of Dice coefficients measuring the similarity between individual functional gradient-derived cognitive spectra and the reference cognitive spectrum. In **c** and **e**, the solid line represents the 50th centile

(median), and the dotted lines represent the 5th, 25th, 75th, and 95th centiles. The growth rate was estimated by the first derivative of the median growth curve, with a 95% confidence interval (shaded in gray) obtained from 1,000 bootstrap resamplings. CI, confidence interval; w, week; m, month; yr, year.

Fig. 6 | Sensitivity analyses of lifespan growth of the sensorimotor-association gradient. a, Lifespan growth curves of gradient measures at the global level. The Pearson's correlation coefficients and mean square errors between the growth curves from the main results and those from the sensitivity analyses are shown in the matrix. For the bootstrap, balanced resampling, and leave-one-site-out analyses, the average growth curves across multiple repetitions are displayed. **b**, Lifespan growth curves of system-level gradient measures. **c**, Lifespan growth of the gradient value for each functional system with peak ages obtained from sensitivity analyses marked by dots in different colors. **d**, Functional system contributions to the lifespan growth of the S-A gradient. For each validation strategy, system contributions across developmental phases were assessed using repeated-measures ANOVA, followed by Bonferroni-corrected post-hoc pairwise t-tests. All statistical tests were two-sided. ***, $p<0.001$. For the bootstrap, balanced resampling, and leave-one-site-out analyses, the results with the median F-value of the interaction effects are presented. **e**, ICC and MMSE maps of the growth rate of the S-A gradient across different validation strategies. **f**, Lifespan growth axes of the S-A gradient obtained from different validation strategies, and their Spearman's correlation coefficients are shown in the matrix. HM, stricter head motion threshold; BSR, bootstrap resampling; SH, random split-half replication; LOSO, Leave-one-site-out; BLR, balanced resampling; MSE, mean square error; VIS, visual; SM, somatomotor; DA, dorsal attention; VA, ventral attention; LIM, limbic; FP, frontoparietal; DM, default-mode; ICC, intraclass correlation coefficient; MMSE, minimal mean square error.

Editor's Summary: This study delineates lifespan changes in the sensorimotor-association gradient using multimodal neuroimaging data from 33,247 participants, revealing a pattern aligned with evolutionary, structural, and cognitive hierarchies within a unified neurodevelopmental framework.

Peer review information: *Nature Communications* thanks the anonymous reviewers for their contribution to the peer review of this work. A peer review file is available.

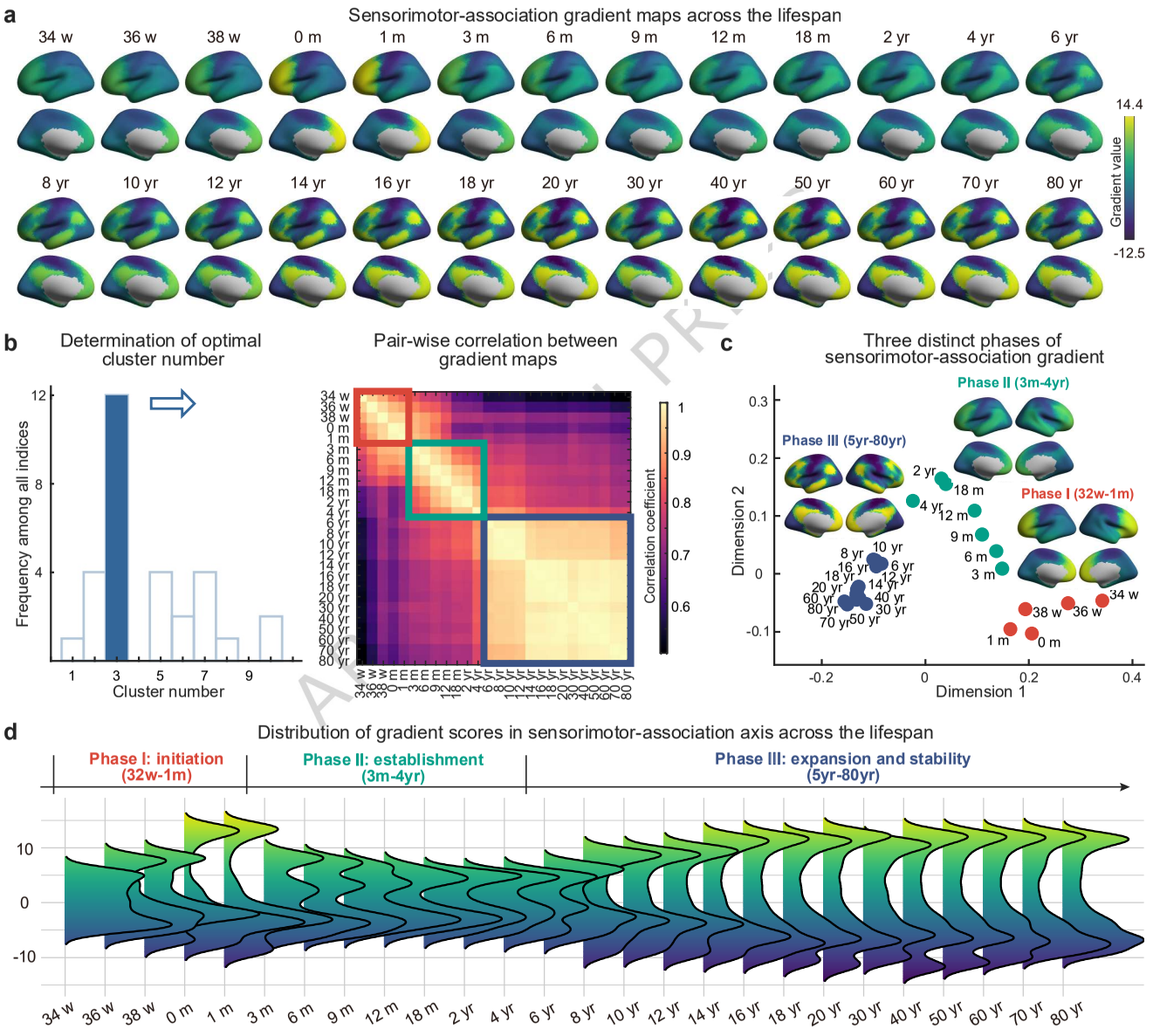
a
Sensorimotor-association gradient maps across the lifespan
34 w
36 w
38 w
0 m
1 m
3 m
6 m
9 m
12 m
18 m
2 yr
4 yr
6 yr
8 yr
10 yr
12 yr
14 yr
16 yr
18 yr
20 yr
30 yr
40 yr
50 yr
60 yr
70 yr
80 yr
14.4
Gradient value
-12.5
b
Determination of optimal cluster number
Frequency among all indices
Cluster number
Pair-wise correlation between gradient maps
Correlation coefficient
c
Three distinct phases of sensorimotor-association gradient
Phase II (3m-4yr)
Phase III (5yr-80yr)
Phase I (32w-1m)
Dimension 1
Dimension 2
d
Distribution of gradient scores in sensorimotor-association axis across the lifespan
Phase I: initiation (32w-1m)
Phase II: establishment (3m-4yr)
Phase III: expansion and stability (5yr-80yr)

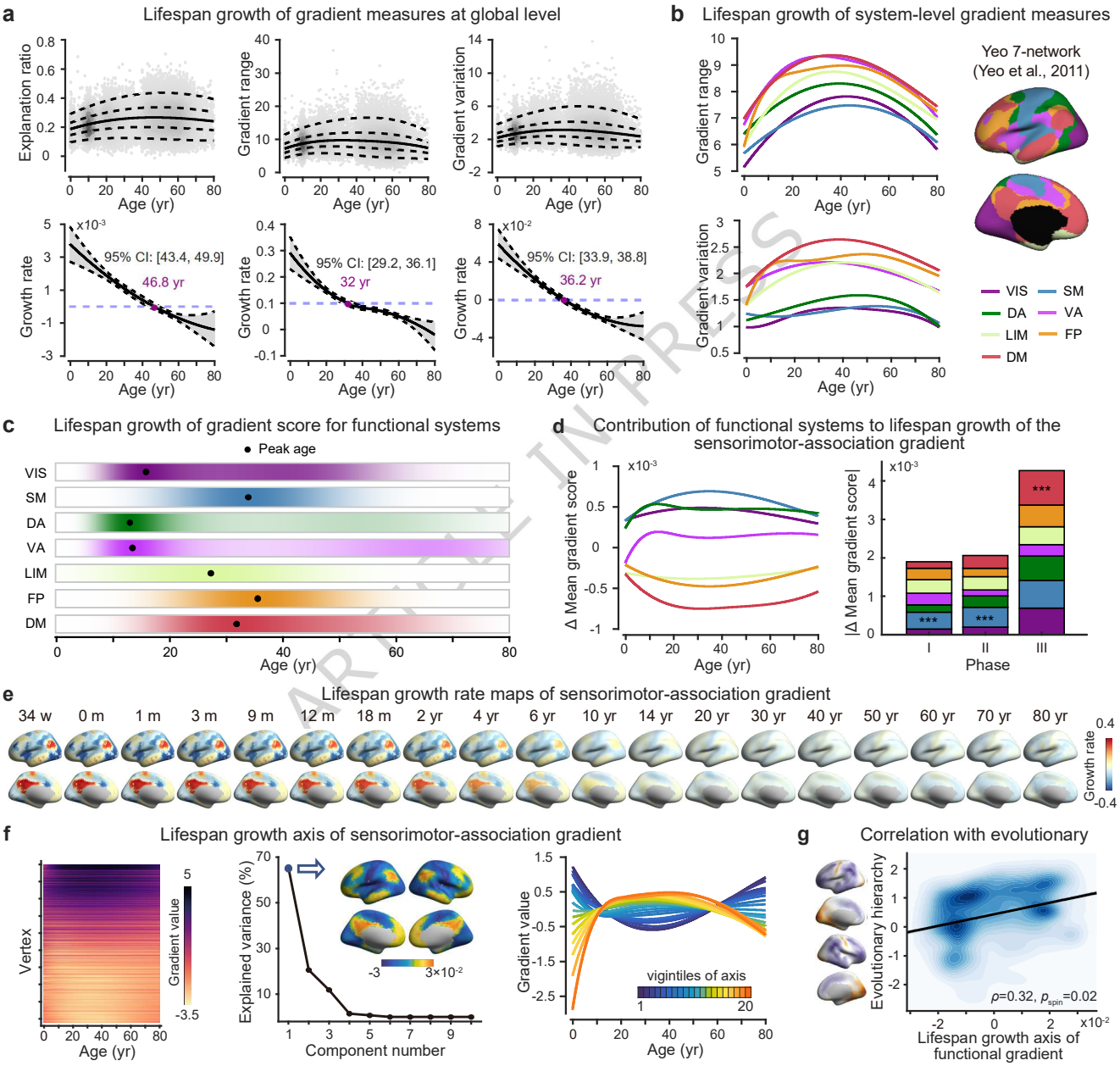

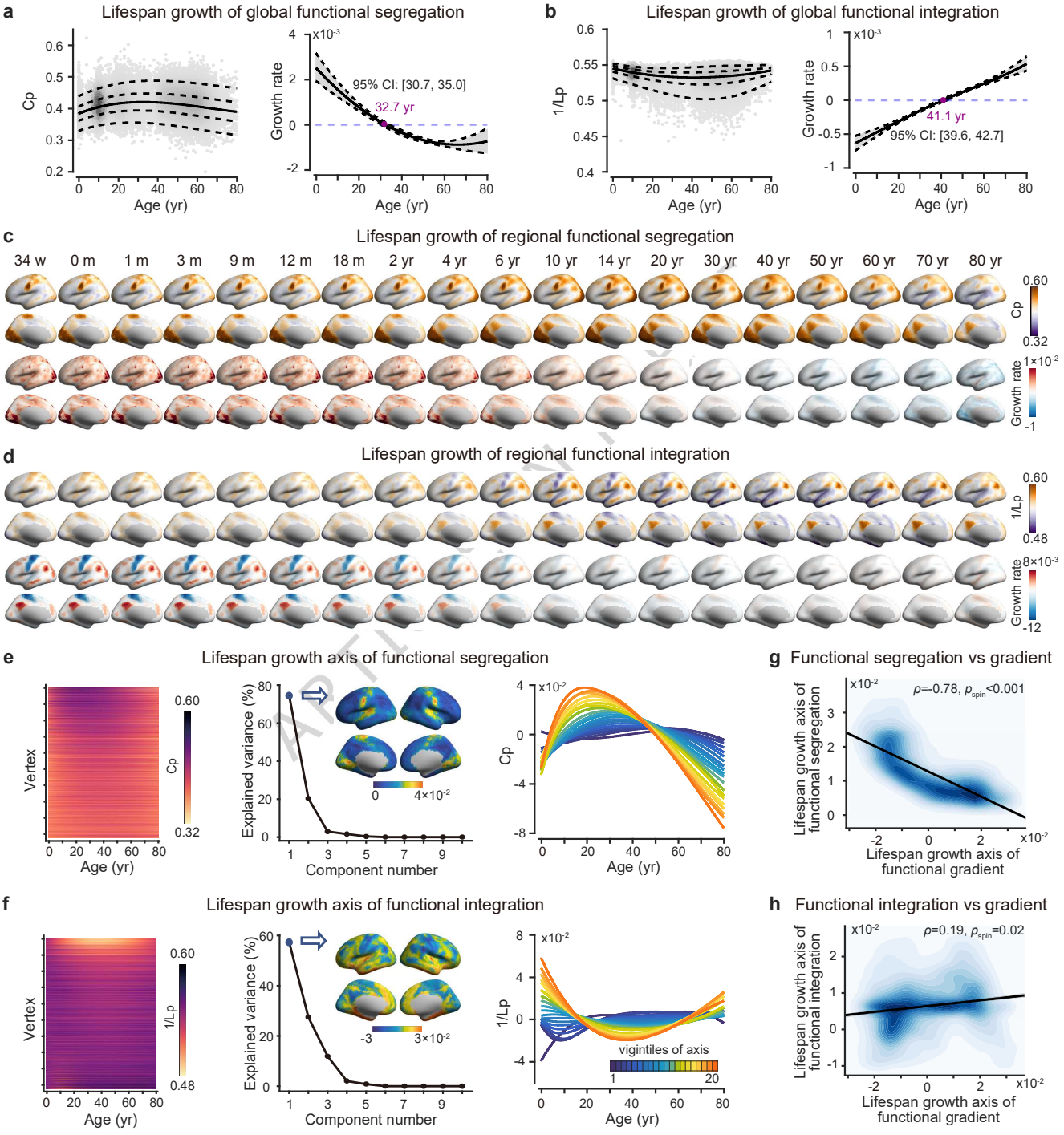
a
Lifespan growth of global functional segregation
Cp
Age (yr)
Growth rate
95% CI: [30.7, 35.0]
32.7 yr
b
Lifespan growth of global functional integration
1/Lp
41.1 yr
95% CI: [39.6, 42.7]
c
Lifespan growth of regional functional segregation
34 w
0 m
1 m
3 m
9 m
12 m
18 m
2 yr
4 yr
6 yr
10 yr
14 yr
20 yr
30 yr
40 yr
50 yr
60 yr
70 yr
80 yr
d
Lifespan growth of regional functional integration
e
Lifespan growth axis of functional segregation
Vertex
Explained variance (%)
Component number
f
Lifespan growth axis of functional integration
vigintiles of axis
g
Functional segregation vs gradient
ρ=-0.78, p_spin<0.001
Lifespan growth axis of functional segregation
Lifespan growth axis of functional gradient
h
Functional integration vs gradient
ρ=0.19, p_spin=0.02
Lifespan growth axis of functional integration

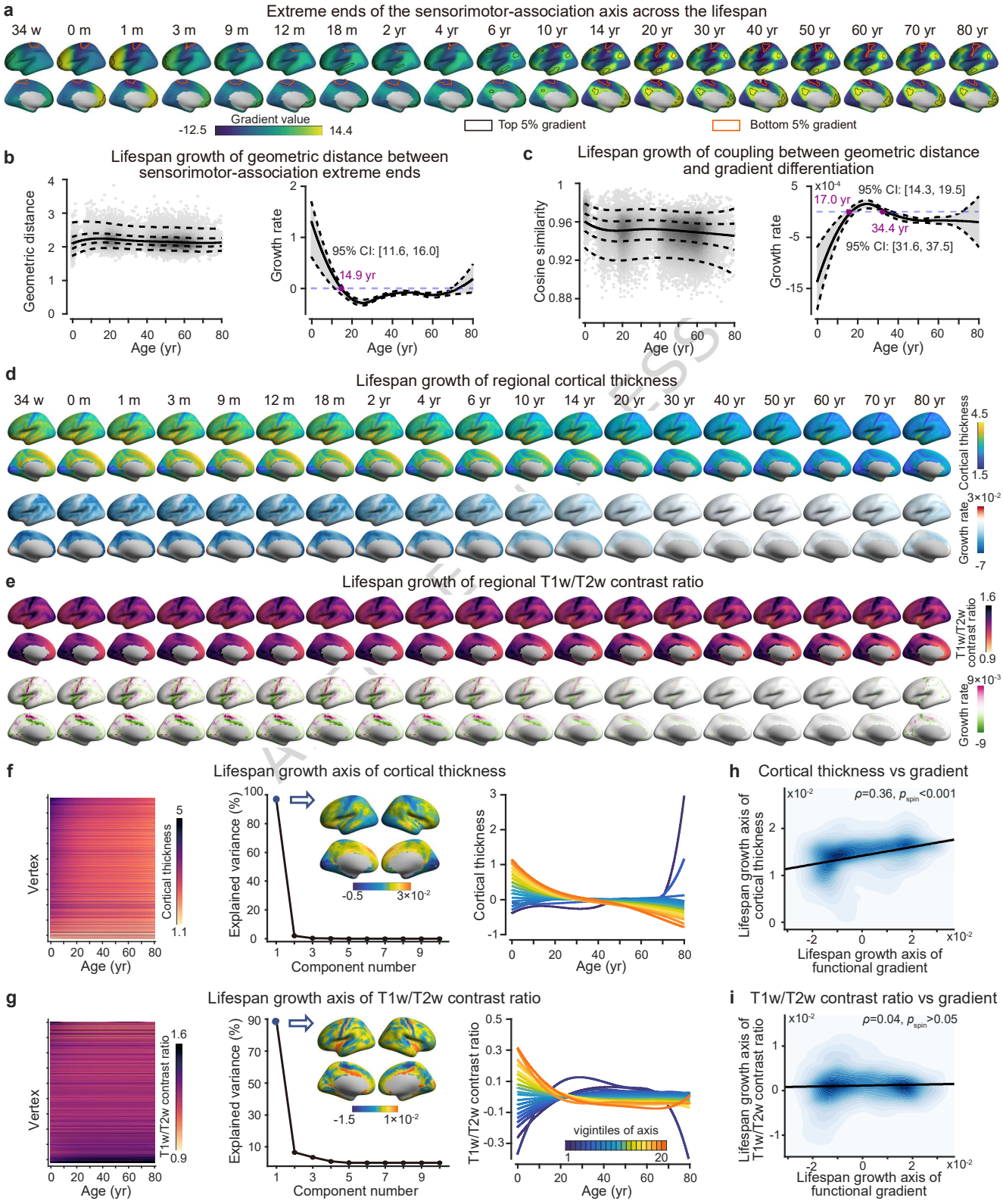
a
Extreme ends of the sensorimotor-association axis across the lifespan
34 w
0 m
1 m
3 m
9 m
12 m
18 m
2 yr
4 yr
6 yr
10 yr
14 yr
20 yr
30 yr
40 yr
50 yr
60 yr
70 yr
80 yr
Gradient value
-12.5
14.4
Top 5% gradient
Bottom 5% gradient
b
Lifespan growth of geometric distance between sensorimotor-association extreme ends
Geometric distance
Age (yr)
Growth rate
95% CI: [11.6, 16.0]
14.9 yr
c
Lifespan growth of coupling between geometric distance and gradient differentiation
Cosine similarity
x10-4
17.0 yr
95% CI: [14.3, 19.5]
34.4 yr
95% CI: [31.6, 37.5]
d
Lifespan growth of regional cortical thickness
Cortical thickness
Growth rate
e
Lifespan growth of regional T1w/T2w contrast ratio
T1w/T2w contrast ratio
f
Lifespan growth axis of cortical thickness
Vertex
Explained variance (%)
Component number
Cortical thickness
h
Cortical thickness vs gradient
ρ=0.36, pspin<0.001
Lifespan growth axis of cortical thickness
Lifespan growth axis of functional gradient
g
Lifespan growth axis of T1w/T2w contrast ratio
i
T1w/T2w contrast ratio vs gradient
ρ=0.04, pspin>0.05
vigintiles of axis